Fermi National Accelerator Laboratory

FERMILAB-Pub-83/26-EXP
7420.616
(Submitted to Nucl. Instrum. and Methods)

MONITORING AND CALIBRATION SYSTEM FOR NEUTRINO FLUX MEASUREMENT IN A HIGH-ENERGY DICHROMATIC BEAM

R. Blair, B. Jin, D. MacFarlane, R. L. Messner,
D. B. Novikoff, and M. V. Purohit
California Institute of Technology, Pasadena, California 91125

P. Auchincloss, F. Sciulli, and M. H. Shaevitz
Columbia University, New York, New York 10027

D. Edwards, H. Edwards, H. E. Fisk, Y. Fukushima, Q. A. Kerns, T. Kondo,
P. A. Rapidis, S. L. Segler, R. J. Stefanski, D. Theriot, and D. Yovanovitch
Fermi National Accelerator Laboratory, Batavia, Illinois 60510

A. Bodek, R. Coleman, and W. Marsh
University of Rochester, Rochester, New York 14627

O. Fackler and K. A. Jenkins
Rockefeller University, New York, New York 10021

November 1983

Monitoring and Calibration System for Neutrino Flux Measurement in a High Energy Dichromatic Beam

R. Blair, B. Jin[a], D. MacFarlane[b], R.L. Messner[c], D.B. Novikoff[d], M.V. Purohit[e]

California Institute of Technology, Pasadena, CA 91125

P. Auchincloss, F. Sciulli, M.H. Shaevitz

Columbia University, New York, NY 10027

D. Edwards, H. Edwards, H.E. Fisk, Y. Fukushima[f], Q.A. Kerns, T. Kondo[f], P.A. Rapidis, S.L. Segler, R.J. Stefanski, D. Theriot, D. Yovanovitch

Fermi National Accelerator Laboratory, Batavia, IL 60510

A. Bodek, R. Coleman[e], W. Marsh[e]

University of Rochester, Rochester, NY 14627

O. Fackler, K.A. Jenkins[g]

Rockefeller University, New York, NY 10021

[a] Institute for High Energy Physics, Peking, Peoples Republic of China.

[b] University of Toronto, M5S187, Canada.

[c] SLAC, Stanford, CA 94305.

[d] Hughes Aircraft Co., El Segundo, CA 90245.

[e] Fermilab, Batavia, IL 60510.

[f] National Lab for High Energy Physics, Tsukuba-gun, Iharaki-ken 305, Japan.

[g] IBM Thomas J. Watson Research Center, P.O.B. 218, Yorktown Heights, NY 10598.

Abstract

In an experiment to measure the cross section for ν-N interactions, the neutrino flux is inferred from measured properties of the secondary hadron beam. The measurements of intensity, composition, and phase space are inputs to a Monte Carlo program which simulates the neutrino beam impinging on the experimental target detector. The components, technical design, and calibration of the devices which monitor the secondary beam are discussed. The accuracy with which the neutrino flux can be determined, given the limitations of the secondary beam monitoring, is also indicated.

I. Introduction

Measurements of neutrino cross sections require knowledge of the incident neutrino flux. The dichromatic, or narrow band, neutrino beam[1] lends itself to measurements from which the neutrino flux can be accurately calculated. This paper describes the instrumentation and method used for neutrino flux determination in a dichromatic beam at Fermilab.[2] The apparatus has been used for several experiments, including a major run (E616),[3] which provided the data for this discussion. The apparatus, with some modifications, has also been used in a recent data taking run (E701, E594).[4] The same techniques will be applied for experiments in the Tevatron beam (E652).

The neutrino beam line at Fermilab is shown schematically in Fig. 1. The neutrino beam is produced through the production and decay of charged pions and kaons. A primary beam of 400 GeV protons impinges on a 30 cm long beryllium oxide target. Among the long-lived collision products (comprising the secondary beam) are π and K mesons. These decay principally via the two-body processes:

$$\pi^{\pm} \rightarrow \mu^{\pm} + \nu_{\mu}(\bar{\nu}_{\mu})$$

$$K^{\pm} \rightarrow \mu^{\pm} + \nu_{\mu}(\bar{\nu}_{\mu}) \quad .$$

The momentum spectrum of the pions and kaons, produced in proton-nucleon collisions, is broad and, if unrestricted, would result in a wide range of neutrino energies. The

narrowing of the meson momentum spectrum is accomplished by means of a series of magnets and collimators, collectively called the dichromatic train (Fig. 2), which follows the BeO target. Secondary particles, selected by charge and by momentum in a range $\Delta P/P \approx 10\%$ (rms) about a mean momentum, P_o, are transmitted by the dichromatic train and pointed toward the neutrino detector. A fraction of the π's and K's decay in an evacuated pipe 350 m long immediately following the train. The resulting neutrino beam has two well defined bands of energy. Neutrinos from π decay may carry up to 43% of the beam energy; those from kaons up to 95%. The kinematics of the decay process lead to a strong correlation between the energy of the neutrino and its transverse position at the neutrino detector. The energy of a muon neutrino produced in a two-body decay is, at high energy,

$$E_\nu = \frac{E_M(1-m_\mu{}^2/M^2)}{(1+\frac{E_M{}^2}{M^2}\theta^2)} \qquad (1)$$

where θ = the angle of emission of the neutrino (with respect to the decaying particle's direction of motion); M = the mass of the decaying particle; E_M = the energy of the decaying particle.

The problem of accurately determining the flux and energy spectrum of neutrinos arriving at the detector becomes one of controlling and measuring the characteristics of the secondary beam. Some properties of this beam, however,

place restrictions on any system used to monitor it. We first give a brief description of the primary and secondary beams and the constraints they impose on the monitoring devices and techniques. This section is followed by a full description of the monitoring system. Finally, the method used to obtain the neutrino flux is outlined.

The 400 GeV primary proton beam is delivered by resonant extraction from the accelerator in "spills" occurring at a rate of approximately 1 every 10 s. They last typically 1 ms or 1 s, depending on the extraction mode (fast or slow spill, respectively) of the accelerator. Most of the running described here occurred during fast spill extraction. The spill has the rf structure of the accelerated beam so that the particles arrive in short bunches (< 2 ns) separated by 18.6 ns. Total primary beam intensity varies from 0.5 to 2.0×10^{13} particles per spill. The proton beam is focused onto a spot (0.5 mm x 2 mm) at the production target.

The secondary beam which emerges from the magnet train has an intensity of 10^9 to 10^{11} particles per spill, depending on the charge and momentum setting. The beam contains several kinds of particles whose proportions depend on setting. Kaons are usually 5% or less of the beam; the pion to proton ratio varies from 1:1 to 1:13 for positive settings over the range 100-250 GeV. On negative settings, the antiproton composition is small (< 2%).

The meson beam has a spread in angles of $\sim$ 0.2 mrad around the mean direction. It exits from the final beam element through an aperture 13 cm x 4 cm. The transverse size of the beam 132 m downstream is approximately 4 cm x 3 cm (rms) at the "expansion port", and is about 6 cm x 7 cm at the "target manhole" which is located 310 m downstream (see Fig. 3).

A 7 m Fe secondary dump at the end of the decay region absorbs the hadronic constituents of the beam. Following the dump, there is 150 meters of steel and 825 meters of earth shielding to stop muons. Behind the shielding is the Lab E enclosure that houses the neutrino detector. A small fraction ($\sim 10^{-9}$) of the neutrinos interact in the 1000-ton Lab E detector.[3,5] At present neutrino beam intensities, this creates roughly one neutrino interaction per spill.

II. Monitoring System

A. Introduction

The apparatus described in this paper was used to measure enough properties of the secondary beam to determine the flux of neutrinos at the neutrino detector to an accuracy of 4%. Further improvements (mentioned below) could reduce the uncertainty by about a factor of two. The flux can be calculated from the following properties of the secondary hadron beam in the decay pipe: the number of pions and kaons in the beam, their direction and position, their decay probability, and their energy. Figure 3 shows the locations

of the monitoring devices along the beam line. The principal monitors are located in the expansion port and the target manhole. A detailed layout of the expansion port instrumentation appears in Fig. 4.

The total intensity of the beam is measured with ion chambers. Beam composition is measured with a Cerenkov counter. The direction of the beam and its angular spread come from profile and position measurements made using ionization devices. The mean energy of the beam is redundantly determined from the total energy of observed neutrino interactions, the beam optics (currents in the dipole magnets), and the Cerenkov counter.

Monitoring devices such as ionization chambers are required to have a response linear with beam intensity over the range of running intensities. The long running time of the experiment requires that all devices also show a high degree of stability. To assure stability, the capability of performing on-line checks was built into the monitoring system. Due to radiation hazards, all devices are remote controlled, and were constructed of materials resistant to radiation damage.

Calibration techniques had to be anticipated, particularly for the total intensity measurement. An important source of calibration data was a special set of runs in which a 200 GeV proton beam was extracted directly from the accelerator and transmitted through the train without targeting. The

momentum of this beam is known to better than 0.5% and its momentum spread is very narrow ($\Delta P/P < 10^{-4}$). The intensity was chosen to be comparable to the intensity of the secondary beam in neutrino running.

B. Electronics

Signals from the various measuring devices used to monitor the beam were sent to nearby counting houses, where they were digitized and stored in CAMAC units. The data were transferred after each spill via the Fermilab beam line monitoring system to the experiment computer in Lab E.

The output of the intensity monitors was digitized using a charge converter which gave a pulse whenever it had integrated a predetermined amount of charge. These charge-to-pulse converters, built at Fermilab, had three different sensitivity ranges (2 picocoulomb/pulse, 20 pc/pulse and 200 pc/pulse).[6] In order to track the stability of the charge digitizers, the more important monitors had a provision to measure a test charge injected between beam spills.

When a neutrino event caused a trigger, the Lab E apparatus was unresponsive to further triggers for about 30 ms. To monitor the flux which passed while the experiment was responsive, signals were sent from the experiment to the flux monitor stations over fast coaxial cables to control live time and dead time gates on the CAMAC scalers. Digital delay of the charge digitizer pulse train was added to accommodate the delay between passage of the beam and receipt

of the gating signals at the monitoring stations. In practice, the ion chambers were not used to measure experiment live time since their response depended on the collection time for positive ions. The primary beam current transformer was used for this purpose, since its response was fast compared to the spill duration. As a check on the gated flux, we monitored special triggers that contained a high purity of neutrino events during live and dead experimental time. This count agreed with the gated monitors to 1% on average for the data taken during the E616 running period.

C. Total Intensity Measurement

1. Primary beam.

The intensity of the primary proton beam was monitored by a secondary emission monitor (SEM),[7] an rf cavity, and a beam current transformer (BCT),[8] all located upstream of the BeO target. Of the three devices, the BCT is the principal monitor of the proton flux. All were used for calibration, for studies of the transmission of the dichromatic train, and for studies of linearity and stability of other flux monitors.

2. Secondary beam.

The principal monitors of the secondary intensity were the ionization chambers located in the expansion port and the target manhole (these chambers will be referred to as XIC and MIC, respectively). The two chambers were similar in construction. They had voltage plateaus several hundreds of volts wide, and operated at 500-700 volts.

The expansion port ionization chamber is shown schematically in Fig. 5. It consists of a cylindrical vessel 20 cm in height and 58 cm in diameter. During operation He gas at atmospheric pressure flowed through the vessel. Within the vessel are Al foils, 80 μ thick, supported by G-10 frames. The active region is 40.6 cm in diameter. The fully assembled structure contains four signal gaps, each a self-contained ionization chamber with a separate collection plane. Voltage planes are supplied from a common source; charge from each signal plane is collected, digitized, and recorded individually. Note that each signal foil is sandwiched between two high voltage plates.

Each gap has a separate function, and gap widths differ accordingly. XIC refers here to the total intensity gap which is 1.25 cm thick. The signal planes of two other gaps, also of width 1.25 cm, are split along a diameter so that charge can be collected separately from the top and bottom halves, in one case, and from left and right halves, in the other. Data from the split-plane gaps were used to monitor beam position (see Sec. D, below). A fourth gap, of width 5 cm, contains a 70 μC americium source, which is an α-emitter, attached to the side wall of the gap. The function of this source gap is to provide information on changes in gas purity and readout calibration.

The ionization chamber in the target manhole (MIC) contains a total intensity gap and two split-plane gaps. The ionization region is 56 cm in diameter, and the gap widths are 0.635 cm. There is no source gap in MIC.

Also located in the expansion port, as shown in Fig. 4, was an rf cavity (XRF) tuned to the accelerator radio frequency, 53.104 MHz. Figure 6 shows a drawing of XRF. The beam passed through the unevacuated region along the cavity axis. The cavity had a loaded Q of 230. The gap impedance (i.e. the voltage induced at the gap per unit beam current at the resonance frequency) was 6100 $\pm$ 100 Ω. This value was obtained by direct measurement using a vector impedance meter (Hewlett Packard 4815A). This agrees within 2% with the value obtained by direct calibration with a proton beam whose intensity was measured by the primary BCT.

The cavity stood on a movable table shared by the Cerenkov counter, which permitted one of the two devices to be in the beam at any given time. Since the rf cavity was a novel device, it took some running to understand and optimize it. In this analysis, the rf cavity was used primarily to calibrate the expansion port ion chamber. For more recent data, taken for E701 and E594, the cavity was used as an independent monitor of beam intensity. The performance of the rf cavity was ultimately encouraging in its stability and reliability, and thus promising as a principal beam monitor in the future. See Fig. 7 for a comparison of XRF

and XIC demonstrating the correspondence of the two.

An attempt to utilize a beam current transformer (BCT) in the secondary beam was made, but failed. The response of the device to the passage of beam halo (particles at wide angles produced when the beam passes through material) through the iron of the toroid produced large spurious signals. It is believed that δ rays also affected the BCT.

3. Linearity and stability.

The two ionization chambers, XIC and MIC, are separated by 120 m; the fact that their support systems, e.g. gas supplies, power supplies, and electronics, are completely independent, provides redundancy in the intensity measurement. The total intensity monitors are cross checked, on-line, for linearity with respect to beam intensity at every energy setting. Figure 8 shows a typical study in which the secondary flux measured by XIC is plotted against the intensity of the primary proton beam as determined by the BCT, over a range of intensities. The ratio XIC/BCT is a measure of the dichromatic beam production and transmission and is expected to be constant at a given energy setting.

Long term stability is demonstrated in Fig. 9, in which the ratio of the intensity recorded by the two secondary beam ion chambers (XIC/MIC) is plotted vs. run number over a running period of about 100 days. During this period, secondary beam energy was changed several times; for about 80% of the period the train was set to transport positive secondaries. Except for the short time near run 1380 when

testing was being done on the ion chambers, the ratio was constant to typically ± 1%. The ratio incorporates the response of each device and its associated electronics. The comparison of XIC to MIC and to the BCT (Fig. 8) indicated that the responses of these devices were stable to better than ± 2% for positive beam and to better than ± 5% for negatives.

4. Ion chamber calibration.

The ionization chambers were calibrated by three methods: the rf cavity, particle counting and foil activation. In the course of calibrating the ion chambers, we discovered that the total ionization observed had a significant correlation with the proton content of the beam. This increase of the output charge with proton fraction may be due to additional ionization produced by interactions in the ion chamber plates. The plates were made of aluminum foil 80 μ thick. Only a very small fraction ($\approx 2 \times 10^{-4}$) of the particles interact in a foil, but an interaction typically results in several heavily ionizing nuclear fragments. Emulsion measurements[9] indicate that typically 1.6 α particles with an energy of approximately 17 MeV and 4 protons of about 10 MeV will be released. Since the interaction cross section is larger for protons than pions, the contribution from interactions will be correspondingly larger for protons. A calculation, based on emulsion data, indicates that 14% of the ionization for protons is due to interactions in the foils. This predicts a 5.5% ± 1.7% difference between

pions and protons, in good agreement with the measured value (6%).

Another difference between pions and protons is the different energy loss in helium due to the difference in velocity of pions and protons of the same momentum. The difference is calculated to affect the response only at the 1% level, and it is opposite in direction to that observed. Effects due to material upstream of the ion chamber were empirically found to be negligible.

An estimate of the ion chamber response, from energy loss in the helium and from contributions of the interactions, differs significantly from the measured value (about 70%). (This estimate depends on the use at high energy of low energy measurements of the number of ion pairs produced per unit energy lost.) This disagreement necessitated careful measurements of the chamber response versus all the relevant parameters (upstream material, particle type and energy).

i) rf cavity. The response of the rf cavity can be calculated from the measured properties of the cavity. Its accuracy was about 5%, limited by the stability, the reliability of the readout technique, and some dependence on rf bucket size. The cavity has the advantages of permitting calibration during neutrino running and of being insensitive to material in the beam as compared with other techniques.

The cavity was operated in air and, to check the effect of the air, studies were performed in a 400 GeV proton beam. A glass beam pipe was used inside the cavity, and the response was measured as a function of gas pressure inside the pipe (see Fig. 10). At low pressure (< 5 microns) and at atmospheric pressure, the cavity response was the same. At intermediate pressures, however, plasma effects reduced the cavity response.

Figure 7 shows the comparison of the rf cavity signal vs. ion chamber response. Such comparisons for the various beam settings with differing proton fractions result in a chamber calibration of $3.47 \pm 0.17 \times 10^{-18}$ coul/particle for mesons and $3.76 \pm 0.22 \times 10^{-18}$ coul/particle for protons. (All calibration values are referred to atmospheric pressure, a temperature of 16° C and 1.25 cm of He.)

ii) Foil activation and primary beam BCT. A second method of calibrating the ion chamber used foil irradiation to measure the train transmission during the 200 GeV proton calibration running. Copper foils were placed in the beam just downstream of the primary beam BCT and just before the ion chamber in the expansion port. The total number of protons entering the train was recorded by the BCT and the transmission of the train was determined by comparing the amount of Na^{24} produced in the upstream foil to that in the downstream foil, by the reaction $p + Cu \rightarrow Na^{24} + X$. The train transmission was measured to be $92.5 \pm 5\%$. This is consistent

with the expected 5% loss from absorption by material in the train and air along the beamline. The upstream foil and BCT yield a measure of the cross section for Na^{24} production on copper by protons of 3.91 $\pm$ 0.2 mb; this may be compared with the value measured at CERN, 3.83 $\pm$ 0.07 mb. The resulting ion chamber calibration is 3.45 $\pm$ 0.22 x 10^{-18} coul/particle (protons).

iii) Particle counting. Two calibration runs were performed in low intensity beams. The particle flux was measured by counting particles in the beam with a scintillator array. The first run was performed in a secondary beam of 275 GeV negative pions of intensity approximately 2 x 10^5 particles/sec. The result of this first run gave 3.57 x 10^{-18} coul/particle for XIC. The accuracy of this calibration was limited by noise in the integrator to about 5%.

The rf cavity data taken during the E616 run had indicated some difference between the ion chamber response to positive and negative secondary beams, respectively, at about the 6% level, as noted above. To study this, a thorough study of the ion chamber response vs. upstream material, beam energy and polarity was performed in the Fermilab M2 beam. By protecting against noise pickup and controlling the beam carefully (e.g., multiple occupancy of rf buckets had to be measured), we achieved a level of accuracy of about 1%.

In order to simulate as closely as possible the actual data taking situation, the amount and location of material in front of the ion chamber under test was identical to that in the decay pipe during neutrino running. Runs were

taken at +90 and +200 GeV, with the material upstream of the ion chamber doubled. The differences in chamber response observed by doubling the material were 0 $\pm$ 1.9% and -2.2 $\pm$ 2% for the +90 and +200 GeV running respectively, consistent with no effect. The measurements clearly rule out upstream material as a significant contributor to the 6% positive/negative ion chamber response difference.

Data were taken at several different secondary energies and both polarities. We concluded from these runs that the calibration was in fact dependent on the secondary beam constitution. By fitting the data with respect to the proton fraction of the beam, it was found that the calibration differed by 6% between mesons and protons (see Fig. 11). No dependence on beam momentum was observed. From these data, the ion chamber response for protons was measured to be 3.62 $\pm$ 0.06 x 10^{-18} coul/particle and for pions it was 3.38 $\pm$ 0.05 x 10^{-18} coul/particle.

The results of the various ion chamber calibrations are shown in Table 1. Averaging the results gives the calibrations used for the flux determination: pions 3.40 $\pm$ 0.05 and protons 3.62 $\pm$ 0.06 coul/10^{18} particles.

D. Beam Shape and Position

The principal monitors recording beam shape and position are segmented wire ionization chambers (SWIC's) located in the primary proton beam before the target and in the secondary beam at the expansion port and the

target manhole. These devices give the vertical and horizontal beam profiles with a resolution of 8 mm. A typical measurement of the beam profile projections at the expansion port and manhole, as measured by the SWIC's, is shown in Fig. 12. Additionally, a small (0.6 cm x 0.6 cm x 1.3 cm) movable scintillator is located in the expansion port. This device is used to scan the beam in horizontal and vertical directions, providing a direct measure of the transverse beam profile. The signal from this scintillator was integrated by a 2 pC/count digitizer of the type described above. A comparison of the beam profile measured by the SWIC in the expansion port and the corresponding profiles constructed from the scintillator data is made in Fig. 13.

Monitoring of the beam direction throughout the experimental running period was done coarsely with the SWIC's, and finely with the split-plane gaps of the two ion chambers. By monitoring the difference between top and bottom, and between left and right plates, the mean neutrino beam position at Lab E was maintained to $\pm$ 2.5 cm throughout the running. Computer monitoring of these differences alerted the experimenters to any shifts in secondary beam position. Such shifts were not frequent; they were typically due to small movement of the primary proton beam on target, when beam extraction changed, exaggerated by the large magnification of the beam optics.

E. Beam Composition

1. Determination of Beam Composition Using the Cerenkov Counter

The secondary beam consists primarily of protons, pions, and kaons. Only pions and kaons contribute to the neutrino flux, and decay probabilities and neutrino energy spectra differ for the two. In order to know the neutrino flux, it is necessary to measure the fraction of pions and kaons in the beam along with the total secondary beam intensity. Determination of the composition of the secondary beam was accomplished using a focusing Cerenkov counter, located in the expansion port and shown in Fig. 14.

The measurement of beam composition with this device differs from its common uses in physics experiments in two important respects: (1) during "fast-spill" extraction, the instantaneous intensity of the secondary beam is about 10^{13} sec^{-1}, precluding the possibility of counting individual particles, and (2) the length of the counter was restricted by the available space, so that the number of photoelectrons per particle was only about 0.005. Each of these factors requiresthat the signal be integrated over the beam spill time and that relative, rather than absolute, numbers of particles be the outcome of the measurement.[10]

The essential elements of the counter are (1) a radiative medium in which coherent light waves are generated in response to a moving charged particle, and (2) an optical system to collect and focus the light. In practice, of course, a vessel is required to contain the medium and to support the optical system. The radiator in this case was 193 cm of He gas. The prominent features of the optical system (Fig. 14) were as follows: the 30.5 cm diameter spherical mirror (M1), of focal length 305 cm; the annular iris, situated approximately 5 cm beyond the focal point; and the photomultiplier tube (PMT), which responded to light in the range 3250-5000 $\mathring{A}$. The iris used in regular data taking transmitted only light emitted at angles of 0.7 to 1.0 mr with respect to the counter axis (also the beam axis). Also of note in the figure is the shutter between the radiative volume of the vessel and the iris, and the auxiliary flat mirrors (M2, M3, M4) which kept the optical path of the Cerenkov counter within the limited space.

The cylindrical vessel itself was constructed of aluminum and had to withstand pressures between 0 and 1 atmosphere.Its upstream end wall was a 0.051 cm thick titanium window through which the beam entered. The interior was painted in flat black. After placement in the beam, the counter's overall position and angle of tilt were adjusted (by remote control) to bring the optical system into alignment with the beam.

The data were obtained by recording the PMT output as a function of He pressure. This was accomplished by filling the counter starting from an evacuated state, with gas released from a small volume injection chamber every other beam spill. The PMT signal and pressure transducer reading were recorded every spill. A sample plot of the Cerenkov photomultiplier response (normalized to the MIC) vs. pressure is shown in Fig. 15. Such Cerenkov curves were taken at every energy setting during the experimental run.

The relation of particle momentum ($\beta = P_{particle} \cdot c / E_{particle}$), index of refraction n, and the angle of Cerenkov light θ_c is given by[11]:

$$\cos\theta_c = 1/\beta n \quad . \qquad (2)$$

The increase in gas pressure, P, increases the index of refraction at these low pressures according to the equation

$$n - 1 = K P \qquad (3)$$

which defines the gas constant, K.

Using the above formulae and applying the approximations

$$\beta \approx 1$$

$$\theta_c << 1 \ ,$$

the Cerenkov relation becomes

$$\theta_c^2 = 2KP - (m/p)^2 \ . \qquad (4)$$

This equation approximates relationship (2) under ideal Cerenkov conditions, which will be defined shortly.

It serves to show the basic relation between particle mass and gas pressure when the angle of the light and the particle momentum are held constant. Under such conditions the number of Cerenkov photons N emitted at θ_c in an interval of wavelength $(\lambda, \lambda+\Delta\lambda)$ is given by

$$\Delta N = 2\pi\alpha \sin^2\theta_c \left(\frac{L}{\lambda}\right)\left(\frac{\Delta\lambda}{\lambda}\right) \qquad (5)$$

where L is the length of the radiative medium, and α is the fine structure constant.

The realization of ideal Cerenkov conditions - parallel, uniform-momentum beam and a very long Cerenkov counter - would result in pressure curves like the one in Fig. 16. The measurement of particle fractions would be obtained from the relative areas of the peaks.

Figure 17 demonstrates how several factors contribute to the broadening of the pion and kaon peaks. With curve (a) representing the ideal counter's response to an ideal beam, curve (b) shows the effect of diffractive interference of light waves in a short radiator.[12] The contributions of the angular divergence and momentum spectrum of the beam are added in curves (c) and (d), respectively. The optical dispersion of the gas has a negligible effect in comparison with the other contributions.

As the figure shows, diffractive broadening is quite pronounced at low pressures, and, in fact, it even results in a signal at full evacuation. Such a signal is predicted by the more general formula for Cerenkov light emitted by a particle moving through a radiator of finite length:

$$dN = C(\lambda)\left(\frac{L}{\lambda}\right)^2 \frac{\sin^2\psi}{\psi^2}\,\theta_c{}^2 d\theta_c{}^2 \qquad (6)$$

where $\psi = \frac{\pi}{2}\cdot\frac{L}{\lambda}\left[\left(\frac{w}{p}\right)^2 - KP + \theta_c{}^2\right]$, and $C(\lambda)$ is a function of wavelength involving the dispersion, $\frac{d\lambda}{d\theta_c}$. The zero pressure signal is transition radiation produced as the beam passes through the end walls of the counter.[12]

The figures show that the momentum spectrum of the beam is the dominant mechanism in broadening of the kaon peak, in contrast to its small effect on the pion peak. In the case of the angular divergence, the reverse is true. Each effect dominates in a different mass pressure region.

It should be noted that the Cerenkov counter sees an angular divergence that is smaller than the beam divergence (as measured by the SWIC's, for example) by roughly a factor of two. The fact that beam is diverging slightly means that it appears to originate from a point source near the secondary production target. While the spherical mirror focuses parallel rays at its focal plane, the sharpest image of any object point is found through the thin lens formula:

$$\frac{1}{f} = \frac{1}{s} + \frac{1}{o} \quad , \qquad (7)$$

where s = the distance from the focusing mirror to the image plane; o = the distance to the object point; f = the focal length of the mirror. For an effective point source a long distance upstream of the counter, the image plane lies slightly beyond the focal plane of the mirror. It was found empirically by moving the iris plane small distances from

the focal plane that the π-K separation could be improved. The pion peak was most narrow for the iris located 5 cm downstream of the focal plane. In this configuration, the Cerenkov counter sees an apparent beam angular divergence given by σ_o = t/s, where t is the apparent source size .

2. Backgrounds

The backgrounds to the Cerenkov data are of four main types. A first source of background, to be referred to as external, is light which is produced outside of the responsive medium of the counter but which is collected in the phototube. This background has several possible sources (e.g. beam halo) but was in any case easily measured. The shutter shown in Fig. 14 was closed for one beam pulse and then opened for one beam pulse at each pressure step; in closed position Cerenkov light produced in the main body of the counter cannot reach the PMT. Figure 15 shows data taken on line with the shutter closed points clearly visible below the signal.

A second background is produced by secondary particles interacting in material directly upstream of the Cerenkov counter including the titanium window of the counter. The radiating medium of the counter is sprayed with a small number of non-beam particles capable of producing Cerenkov light. As an empirical measure of this background, special curves were taken with extra material in the beam at two beam settings (120 and 250 GeV, negative charge) and during the 200 GeV proton calibration tests. The amount of material

directly upstream of the counter, during normal running, including the door to the decay pipe, the counter's titanium window, and air, was the equivalent of 0.2 cm of titanium, or 0.007 of an interaction length. The extra material was 1.3 cm aluminum in three cases and 0.5 cm titanium in a fourth case, adding 0.03 or 0.02, respectively, of an interaction length. It has further been shown that the background rises linearly with the amount of material.

Figure 18 shows a pressure curve from which the external background has been subtracted. The lower curve results from the subtraction of the material-out curve from the material-in curve, and the difference has been normalized to the amount of material normally in the beam.

To investigate the possible contribution of beam-material interactions far upstream of the counter, a simple Monte Carlo calculation was performed. The plot in Fig. 19 shows the result of simulating pion interactions in 0.03 interaction lengths of material. The two curves correspond to different angular ranges for the material-induced secondaries: the full solid angle in the upper curve and between 0-1 mrad in the lower. The upper curve reproduces the measured background to roughly a factor of two over the entire pressure range. The lower curve would correspond to interactions occurring at the entrance to the decay pipe, the next upstream position at which material is located (132 m from the counter. Because of the small solid angle subtended by the Cerenkov counter at this distance,

upstream interactions by even several percent of the beam would contribute less than ~ 1% to the background actually observed between the peaks and beyond the proton peak.

Interactions in the material close to the counter could conceivably produce non-linear effects, such as low energy delta rays. This contribution was calculated and found to be negligible.

Other particles, besides the predominant π's, K's, and protons in the secondary beam constitute a third background. Electrons (or positrons) and muons are produced at the beryllium oxide target and may be transported in the beam. Furthermore, a predictable fraction of π's and K's decay in the 132 m region between the end of the magnet train and the Cerenkov counter. Their decay products, mainly π's and μ's, contribute a background distributed in accordance with the kinematics of the decay process. The Cerenkov light resulting from K-decay processes as calculated by Monte Carlo is shown in Fig. 20. The contribution of muons from pion decay is small and, because of proximity in mass, the signal from these muons cannot be separated from that of the pions. Electrons which are on momentum can be partially distinguished from pions at or below 140 GeV/c. The e/π ratio was estimated by a Monte Carlo calculation simulating electron production at the target. The data available at 120 GeV and above agreed to 1% with the calculated values.

The fourth background has been attributed to light which scatters off dust particles in the gas or on the mirrors and finds its way past the iris. Evidence for a background is seen in a high pressure tail extending beyond the proton peak even after subtraction of the material and external backgrounds. The major evidence for its origin is that when one of the mirrors was cleaned mid-run, the level of the high pressure tail immediately diminished, and the level was observed to rise slowly with time thereafter. The general properties (pressure dependence, etc.) of this residual background are consistent with those of light diffractively scattering from small dust particles.

A problem introduced by the Cerenkov counter itself was that the counter bowed slightly as pressure was increased. The iris was therefore displaced with respect to the focused Cerenkov rays and the signal noticeably distorted. The angular deflection of iris with pressure was measured after the experimental run and was found to be very reproducible; data from these studies are shown in Fig. 21.

3. Analysis of Cerenkov Data

The analysis was aided by additional data collected in order to study systematic effects. The 200 GeV calibration beam was used to obtain the gas constant (K in Eq.4) and to observe the counter's response to a beam with a small momentum spread. Data were taken with additional material in the beam

at 250 and 120 GeV negative settings (see Sec. E.2). From these Cerenkov curves, the material background at other energies was found by interpolation. At all energy settings, several curves were taken and these duplicate curves revealed the time dependence of the residual high pressure tail. Special data were obtained at 90 GeV to help determine the electron fraction of the beam.

Particle fractions were calculated by fitting simulated Cerenkov response functions, generated by Monte Carlo calculation, to the actual data. The calculation was based on the general (non-ideal) Cerenkov equation given above and incorporated diffraction, beam phase space, particle decays, and the iris motion.

The external background and the interpolated material background were subtracted from the data before fitting. Two schemes were devised to parametrize the light scattering background. These led to particle fractions which differed typically by 2%. The final scheme allowed the amplitude of each simulated peak and the background to be adjusted in the fitting program. Figure 22 illustrates the fit of the linear combination of all response functions to data at 168 GeV, positive beam. Included are the light scattering background, the separate π, K and proton peaks, and the total. The considerable overlap, due to diffraction, of the tails of individual particle peaks shows why a method like this is preferable to one based on

the relative areas under the peaks in the data. The data and Monte Carlo fits at all energy settings are presented in Fig. 23.

We estimate that the particle fractions obtained in this analysis were accurate to within 1-4% for π's and 4-7% for kaons. The unknown, detailed shape of some material and light scattering backgrounds and the small fraction of K's in the beam are the main causes for the level of precision. In a more recent experiment (E701, E594) with a newly built Cerenkov counter, several improvements were introduced. More data were taken with extra material so that it is no longer necessary to interpolate the material background. The new counter was designed with fewer mirrors, a gentler gas inlet valve, and a smoother shutter motion, in an effort to reduce the dust. The problem of iris motion was eliminated by supporting the optics on a frame distinct from the walls of the pressure vessel.

In Table 2 we have tabulated the kaon to pion ratios. A correction has been made to adjust this ratio to the production target (i.e., decays downstream of the target have been compensated). The number of secondary particles produced and transmitted, per proton on target, is plotted in Fig. 24. All of these values depend, of course, on the acceptance in angle and momentum of the dichromatic beamline.

IV. Neutrino Flux

A. Monte Carlo

The neutrino-nucleon cross section for $\nu_\mu + N \rightarrow \mu + X$ is known to increase linearly with respect to the energy of the neutrino, that is:

$$\frac{d\sigma}{dE_\nu} \approx \text{constant} \quad . \qquad (8)$$

The number of events observed in the detector is therefore expected to be proportional to the energy-weighted neutrino flux $\tilde{\phi}_\nu$:

$$\tilde{\phi}_\nu(R) = \int \phi_\nu(R) E_\nu dE_\nu \qquad (9)$$

R = the distance from beam center at Lab E.

where ϕ_ν = the flux of neutrinos per unit energy, and E_ν = the neutrino energy. The quantity $\tilde{\phi}_\nu$ in turn depends on the phase space of the secondary beam, the total number of secondaries, and the kinematics of two-body decays of pions or kaons.

One method of calculating the neutrino flux is to model the proton beam targeting, secondary production[13] and transmission of the dichromatic train. The number of neutrinos, per particle observed at the monitoring locations, may then be computed using secondary beam phase space derived from the model. This was taken as a starting point. The model beam's characteristics were then adjusted to agree with those measured in the real beam. The result should therefore be almost independent of such poorly measured quantities as the exact size of the proton spot on the target, the shape of the production spectrum in momentum and angle, and the

positions of the magnets.

The effect of the spatial and momentum distributions of the secondary beam particles on the neutrino energy spectrum may be demonstrated by comparison with the spectrum calculated for a monoenergetic, on-axis beam. First of all, an error in the determination of the mean energy of an ideal beam affects $\tilde{\phi}_\nu$ as shown in Fig. 25, where $\Delta\tilde{\phi}_\nu$ is plotted versus radius at Lab E. Figure 26 shows how the momentum dispersion, angular dispersion, and a spread in position, affect the value of $\tilde{\phi}_\nu$. Each factor has been introduced separately and at a level expected for E616.

1. Mean Beam Momentum

For high energy neutrinos from kaon decays, the most important quantity in determining the neutrino flux is the mean energy of the secondary beam. This can be determined in two ways. The first uses measurements on the secondary beam taken with the Cerenkov counter. From the formula for emission of Cerenkov light, we can express the average pressure in terms of the average of $1/p^2$:

$$\langle \mathcal{P} \rangle = \frac{m^2 \langle 1/p^2 \rangle + \theta_o^2}{2K} \qquad (10)$$

where θ_o = the effective Cerenkov angle of the iris. The value of θ_o in the above expression can be obtained by finding the intercept for pions in a plot of $\langle \mathcal{P} \rangle$ vs. $\langle 1/p^2 \rangle$ (see Fig. 27). Since the angular dispersion of the beam may affect the apparent value of θ_o, the error on the momentum

is increased; the resultant uncertainty for pions is $\sim$ 5% and for kaons it is $\sim$ 0.5%. Because the Cerenkov data yield $\langle 1/p^2 \rangle$, the last step in obtaining the average momentum requires computation of the factor $\langle p \rangle \times \sqrt{\langle 1/p^2 \rangle}$ using a Monte Carlo program.

The second method of measuring the mean energy of the secondary beam is by observing the mean energy of neutrinos which are emitted at small angles from the beam direction. When a neutrino interaction occurs at the detector the hadron energy and the muon momentum are measured. The hadron energy calorimetry was calibrated by moving pieces of the target into a hadron beam of precisely known energy. The magnetic field of the muon spectrometer was measured using a Hall probe. Based on the calibration and field measurements, the total energy of neutrinos may be determined from hadron energy and muon momentum with a precision of about 2%. Restricting the sample to pion decay neutrino events within 25 cm and kaon decay neutrino events within 127 cm of the center of the beam, the average neutrino energy is approximately proportional to the beam momentum.

A comparison between the two methods of obtaining the beam energy appears in Fig. 28. The adjustments to the values predicted by the model beam were: 0.7% for π^+, -0.1% for π^-, 2.2% for K^+, and 0.9% for K^-. (These values are averaged over the five secondary settings and show little dependence on setting.)

2. rms Momentum Dispersion σ_p and rms Angular Dispersion.

The momentum spread of the beam is measured with the Cerenkov data in a manner similar to that described for the mean momentum. The width of the peak of a Cerenkov pressure curve may be translated into the width of the momentum spectrum. This technique was applied to the kaons and the momentum bite from the Monte Carlo agreed to better than 1% with the measurement.

The SWIC profilers at the expansion port and target manhole and the size of the aperture at the end of the train provide rough information about the angular dispersion of the beam. The model's prediction of σ_θ did not always agree with estimates from measured quantities, but agreement was sufficient to calculate $\tilde{\phi}_\nu$ to better than 5% for pion decay neutrinos and better than 1% for kaon decay neutrinos.

3. Backgrounds

There are two sources of non-dichromatic neutrinos, that is neutrinos for which energy and angle are not uniquely correlated as in the case of the two-body decays of pions and kaons. First, neutrinos are produced upstream of the decay pipe. These upstream sources can be isolated by closing the collimating slit at the end of the train and dumping the secondary beam before it enters the decay pipe. About 10% of our running was done in this mode. The number of events

observed at Lab E during closed slit running showed a linear rise both with the solid angle subtended at the neutrino detector and with the number of protons on target (see Fig. 29).

Kaon decay modes other than the $K \rightarrow \mu\nu$ decay mode comprise the second source of background neutrinos. The most significant decay modes are $K \rightarrow \pi^o\mu\nu$ and $K \rightarrow \pi^o e\nu$. The contribution from these decays is calculated using the beam phase space as determined for the two-body decay modes. A comparison of the various decay contributions appears in Fig. 30.

V. Summary

By measuring all of the relevant properties of the charged secondaries (pions and kaons), we have been able to determine neutrino fluxes with an accuracy that is reasonably well matched to the statistics of our event sample. A summary of the errors estimated from various sources along with the statistical error for our charged current events appears in Table 3. As mentioned, improvements have been made in the monitors, which may further reduce some of the errors.

We would like to express our gratitude to the Fermilab staff for assistance in the construction and maintenance of the beam line monitoring apparatus. We would also like to thank Stephen Pordes for his very helpful suggestions regarding this article. This research was partially supported by the National Science Foundation and the Department of Energy.

References

1 F. Sciulli et al, "Neutrino Physics at Very High Energies", Fermilab Proposal 21 (FNAL) 1970; V. Peterson, "A Monochromatic Neutrino Beam from a High Intensity 200 GeV Proton Synchrotron", LRL Report UCLD-10028 (1964).

2 D. Edwards, F. Sciulli, "A Second Generation Narrow Band Neutrino Beam", TM-660, Fermi National Accelerator Laboratory (1976).

3 R. Blair et al, Phys. Rev. Lett. 51, (1983) 343.

4 I. Stockdale et al, "Limits on Muon Neutrino Oscillations in the Mass Range $20 \ll \Delta m^2 < 900$ eV^2", University of Rochester preprint UR-860 (1983)(submitted to Phys. Rev. Lett.); L. Stutte et al, "Early Results from E594. A Fine Grained Neutrino Detector", Proceedings of Neutrino '81, Vol. 12, p. 377-87.

5 R. Blair, "A Total Cross Section and Y Distribution Measurement for Muon Type Neutrinos and Antineutrinos on Iron", Ph.D. Thesis, Caltech (1982); J. Lee, "Measurement of νN Charged Current Cross Sections from E_ν = 25 GeV to E_ν = 260 GeV", Ph.D. Thesis, Caltech (1981).

6 A.R. Donaldson, IEEE Trans. Nucl. Sci. NS-26, (1979) 3439.

7 Made by L.N.D. Inc., 3230 Lawson Blvd., Ocean Side, NY 11572.

[8] C.R. Kerns, "Radiation Hardened Proton Meter for Fermilab External Beam Lines", TM-551, Fermi National Accelerator Laboratory (1975).

[9] C.F. Powell, P.H. Fowler, D.H. Perkins, The Study of Elementary Particles by the Photographic Method, pp. 424-471, Pergamon Press (1959).

[10] J.G.H. deGroot et al, Z. Phys. C - Particle and Fields 1 (1979) 143; Phys. Lett. 82B (1979) 292, 456; M. Holder, J. Steinberger, CERN rep. NP/JS/ih/125 (1974).

[11] J. Litt, R. Meunier, Ann. Rev. Nucl. Sci. 23 (1973) 1.

[12] A. Bodek et al, "Observation of Light Below Cerenkov Threshold in a Short Cerenkov Counter", Z. Phys. C 18 (1983) 289-299.

[13] H.W. Atherton et al, "Precise Measurements of Particle Production by 400 GeV/c Protons on Beryllium Targets", CERN Preprint, CERN 80-07 (1980).

Table 1: Various calibrations of the expansion port ion chamber (XIC) total intensity gap. All values are referred to 1 atm He, and T = 16° C.

Method	Response (10^{-18} coul/part)
Counting 275 GeV π^-	3.57 ± 0.18
Foil Irradiation: 200 GeV p	
(a) CERN BCT	3.38 ± 0.22
(b) FNAL BCT	3.45 ± 0.22
rf Cavity	
protons	3.76 ± 0.22
pions	3.47 ± 0.17
Counting	
protons	3.62 ± 0.06
pions	3.38 ± 0.05
Response Used	
protons	3.62 ± 0.06
pions	3.40 ± 0.05

Table 2: Ratio of the number of kaons to pions which pass through the train to the decay pipe. A correction has been made to compensate for decays after the production target.

Setting	Positive K to π Ratio	Negative K to π Ratio
120	0.108 $\pm$ 0.008	0.0714 $\pm$ 0.0040
140	0.119 $\pm$ 0.007	0.0767 $\pm$ 0.0031
168	0.128 $\pm$ 0.007	0.0696 $\pm$ 0.0023
200	0.140 $\pm$ 0.009	0.0533 $\pm$ 0.0020
250	0.164 $\pm$ 0.011	0.0450 $\pm$ 0.0020

Table 3: Error on $\tilde{\phi}_\nu$ resulting from uncertainties in secondary beam properties. For comparison the range of statistical error is shown for events from kaon decay with interaction vertex less than 127 cm from the beam axis, and from pion events with vertex less than 64 cm from beam center. The ion chamber calibration category includes any uncertainties in applying the calibration run to the two running periods (positive and negative). The ion chamber stability category includes the dead time uncertainty.

	Neutrinos from π^+	Neutrinos from π^-	Neutrinos from K^+	Neutrinos from K^-
Particle fractions	4%	1%	5-6%	4-6%
Uncertainty in secondary momentum	1-3%	1-3%	1-2%	1-2%
Uncertainty in secondary beam σ_θ	1-5%	1-5%	1%	1%
Ion chamber calibration	3%	6%	3%	6%
Ion chamber stability	3%	5%	3%	5%
Event statistics (for comparison)	1-2%	2-3%	1-5%	5-8%

Figure Captions

Fig. 1 Location of the dichromatic beam channel, monitor ports, and Lab E detector along the Fermilab neutrino beam line.

Fig. 2 Schematic diagram of the dichromatic magnet train, illustrating the bending of the secondary hadron beam. The first four dipole magnets (D1-4) are rotated about the beam direction, causing bending in both the horizontal and vertical views. The angles of rotation are: D1 - 12° CCW; D2 - 30° CCW; D3 - 24° CCW; and D4 - 20° CW.

Fig. 3 Location of the primary and secondary beam monitoring devices along the neutrino beam line.

Fig. 4 Plan of the expansion port, top and side views. The rf cavity and the Cerenkov counter share the same movable table, allowing one or the other to be placed in the beam by remote control. An ion chamber and SWIC are permanently situated in the beam. The scanning scintillator is movable in the transverse directions. Gas supplies and electronics are located in a building outside.

Fig. 5 Schematic diagram of the ion chamber in the expansion port. The signal from each gap is digitized separately, and each digitizer is individually calibrated.

Fig. 6 rf cavity. The cavity is a folded 20 ohm coaxial transmission line, with one end shorted to form a quarter wave resonator, constructed of pure aluminum. (1) is the gap excited by the rf structure of the beam; (2) is a magnetic loop tap.

Fig. 7 rf cavity signal vs. ion chamber signal over a range of secondary beam intensities, in a test of device linearity.

Fig. 8 Ion chamber signal vs. primary beam intensity as measured by the (primary) BCT.

Fig. 9 The ratio of the target manhole ion chamber signal to expansion port ion chamber signal vs. run number. The plot demonstrates the long-term stability in the ion chambers' responses.

Fig. 10 The response of the rf cavity vs. the pressure of the air in the gap.

Fig. 11 Ion chamber response vs. fractional proton content of the secondary beam.

Fig. 12 Data from two segmented wire ion chambers (SWIC's) showing beam profiles at the two monitor ports.

Fig. 13 Comparison of the beam profilestaken by the expansion port SWIC and constructed from the scanning scintillator data.

Fig. 14 Cerenkov counter used in experiment E616.

Fig. 15 Cerenkov data taken at 168 GeV, with positive beam. The upper set of points is the raw signal (that is, phototube output normalized by ion chamber signal) with the shutter open; the lower set is the signal with the shutter closed, eliminating light from the radiator of the counter.

Fig. 16 Plot depicting how Cerenkov data would appear under ideal conditions at 100 GeV.

Fig. 17 An illustration of the effects on the Cerenkov counter's response to successive deviations from ideal conditions. (a) Ideal Cerenkov conditions - ideal beam and very long counter; (b) short counter; (c) angular divergence of the beam; and (d) momentum spectrum of the beam.

Fig. 18 Empirical measure of the background due to interactions of the beam in material just upstream of the Cerenkov counter. The upper curve comes from data from which the external background has already been subtracted. The lower curve is the difference of extra material-in and-out curves, scaled to the level caused by material normally in the beam.

Fig. 19 Monte Carlo simulation of the material background at the Cerenkov counter. The two curves show approximately effect of material at a distance within 3 m upstream of the counter (dashed line) and at about 132 m upstream of the counter.

Fig. 20 Background due to the decays of kaons upstream of the Cerenkov counter, as calculated by a Monte Carlo. (a) Kaon signal without decay products; (b) background produced by decay products.

Fig. 21 Angular deviation of the iris from its correct position, versus pressure. The deviation was caused by the flexing of the counter optics.

Fig. 22 Cerenkov curve at 168 GeV, positive beam, showing data, fitted Monte Carlo curves for pions (a), kaons (b), and protons (c); light scattering background (d) and the sum (e).

Fig. 23 Cerenkov data and fits at all experimental beam settings.

Fig. 24 Number of each type of secondary particle at the production target normalized to the number of incident protons, vs. momentum setting.

Fig. 25 The shift in $\tilde{\phi}_\nu$ (flux x energy) that would result from using the wrong energy (high by 1%). The upper curve is for pions, the lower for kaons. This shift is calculated for a perfect 200 GeV secondary beam.

Fig. 26 The shift in $\tilde{\phi}_\nu$ (flux x energy) caused by various deviations from a perfect 200 GeV beam. Each change is applied alone. The dashed line shows the effect of a rms angular dispersion of 0.25 mrad. The dotted line shows the effect of a finite beam size, rms deviation of 4 cm in x and y. The solid lines show how a gaussian momentum

distribution (rms deviation of 9.6%) changes $\tilde{\phi}_\nu$.

Fig. 27 Average pressure vs. average m^2/p^2. The value of $\langle 1/p^2 \rangle$ is evaluated by using the mean neutrino energy of pion decay neutrinos, as seen at the neutrino detector, with interaction vertex less than 25 cm from the central beam axis.

Fig. 28 Momentum of the secondary beam as determined from Cerenkov curves (black boxes) and neutrino data (open boxes). The momentum is expressed in percent difference from the train's nominal setting.

Fig. 29 The number of closed slit events observed, vs. distance from beam center, and vs. number of primary protons.

Fig. 30 Results of a Monte Carlo calculation of the relative number of neutrino events from two body and three body decays. The energy setting for this plot is 200 GeV.

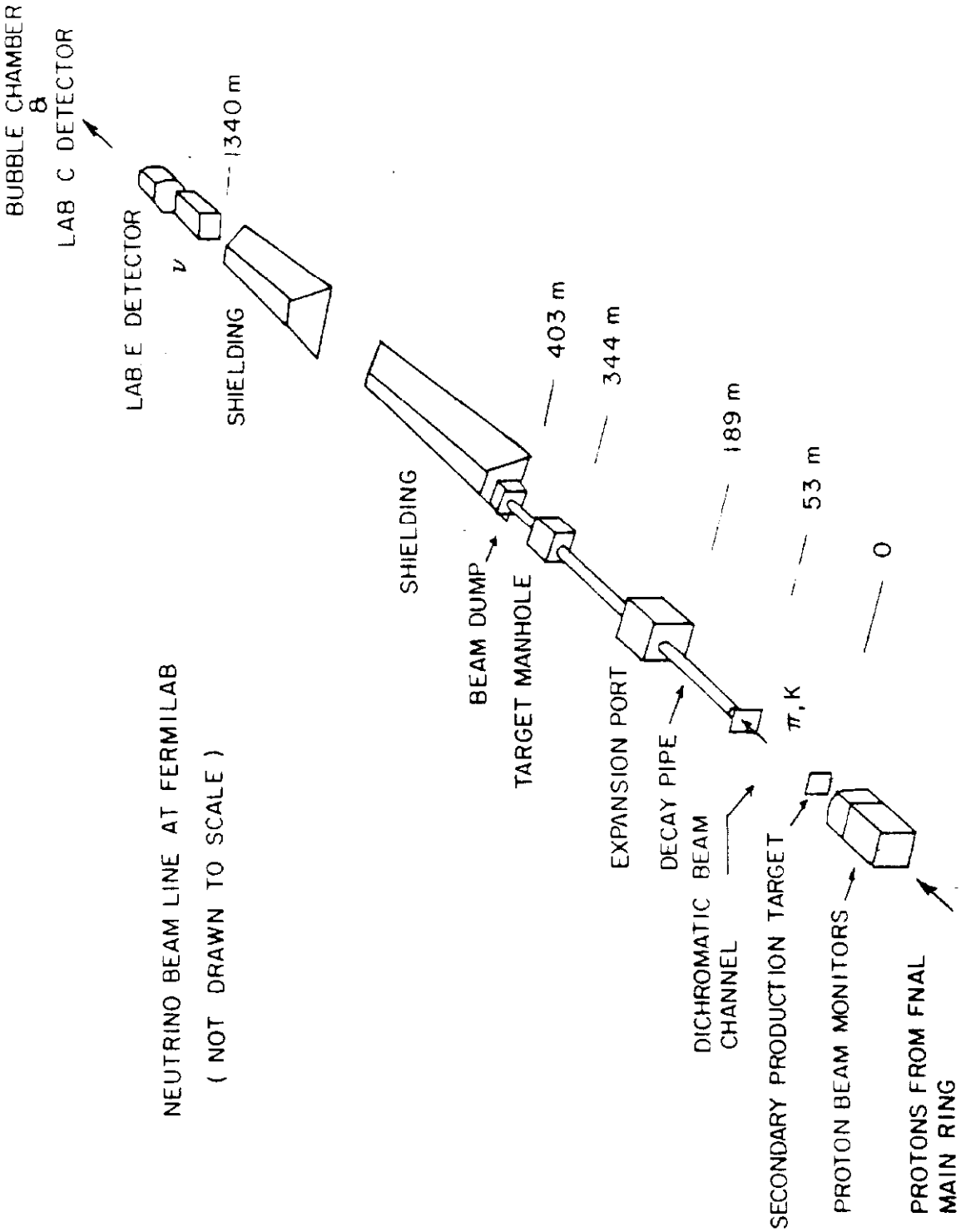
BUBBLE CHAMBER
&
LAB C DETECTOR
LAB E DETECTOR
ν
1340 m
SHIELDING
NEUTRINO BEAM LINE AT FERMILAB
(NOT DRAWN TO SCALE)
SHIELDING
403 m
344 m
189 m
53 m
0
BEAM DUMP
TARGET MANHOLE
EXPANSION PORT
DECAY PIPE
DICHROMATIC BEAM
CHANNEL
π, K
SECONDARY PRODUCTION TARGET
PROTON BEAM MONITORS
PROTONS FROM FNAL
MAIN RING

Figure 1

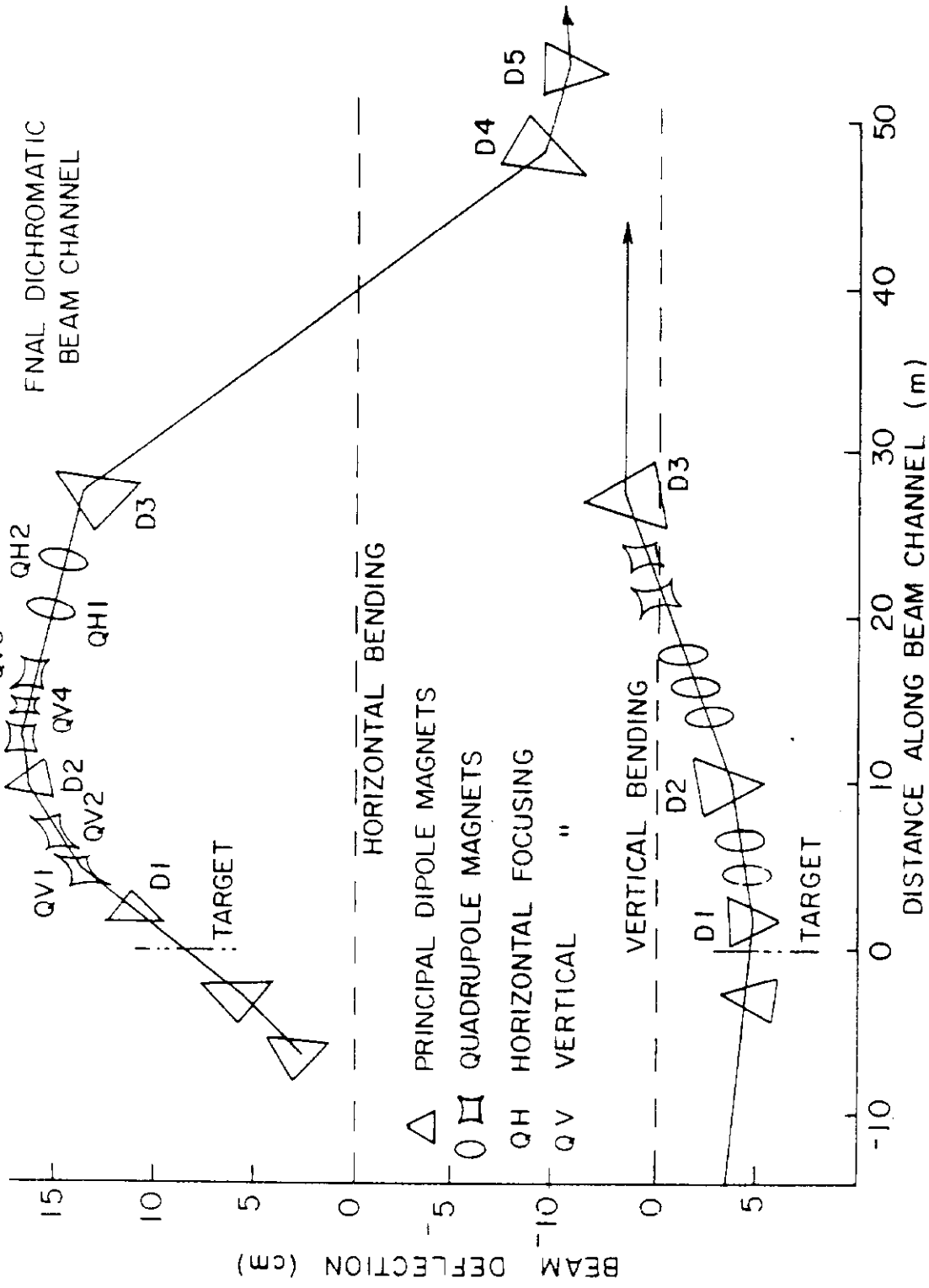
FNAL DICHROMATIC
BEAM CHANNEL
QV1
QV2
D2
QV3
QV4
QV5
QH1
QH2
D1
TARGET
D3
D4
D5
HORIZONTAL BENDING
VERTICAL BENDING
PRINCIPAL DIPOLE MAGNETS
QUADRUPOLE MAGNETS
QH HORIZONTAL FOCUSING
QV VERTICAL "
BEAM DEFLECTION (cm)
DISTANCE ALONG BEAM CHANNEL (m)
15
10
5
0
-5
-10
-10
0
10
20
30
40
50

Figure 2

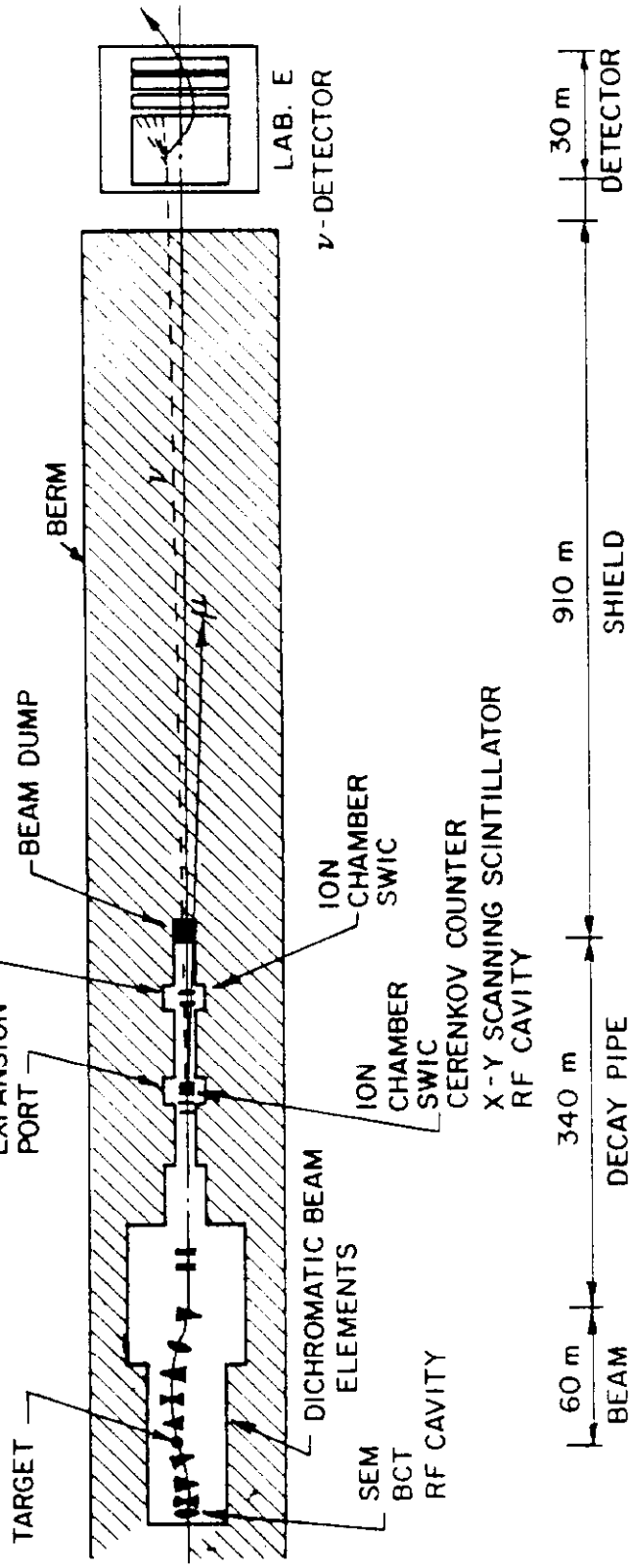
TARGET MANHOLE
BEAM DUMP
BERM
LAB. E
ν - DETECTOR
EXPANSION PORT
ION CHAMBER SWIC
ION CHAMBER SWIC
CERENKOV COUNTER
X - Y SCANNING SCINTILLATOR
RF CAVITY
DICHROMATIC BEAM ELEMENTS
TARGET
SEM
BCT
RF CAVITY
60 m
BEAM
340 m
DECAY PIPE
910 m
SHIELD
30 m
DETECTOR
FNAL NEUTRINO BEAMLINE

Figure 3

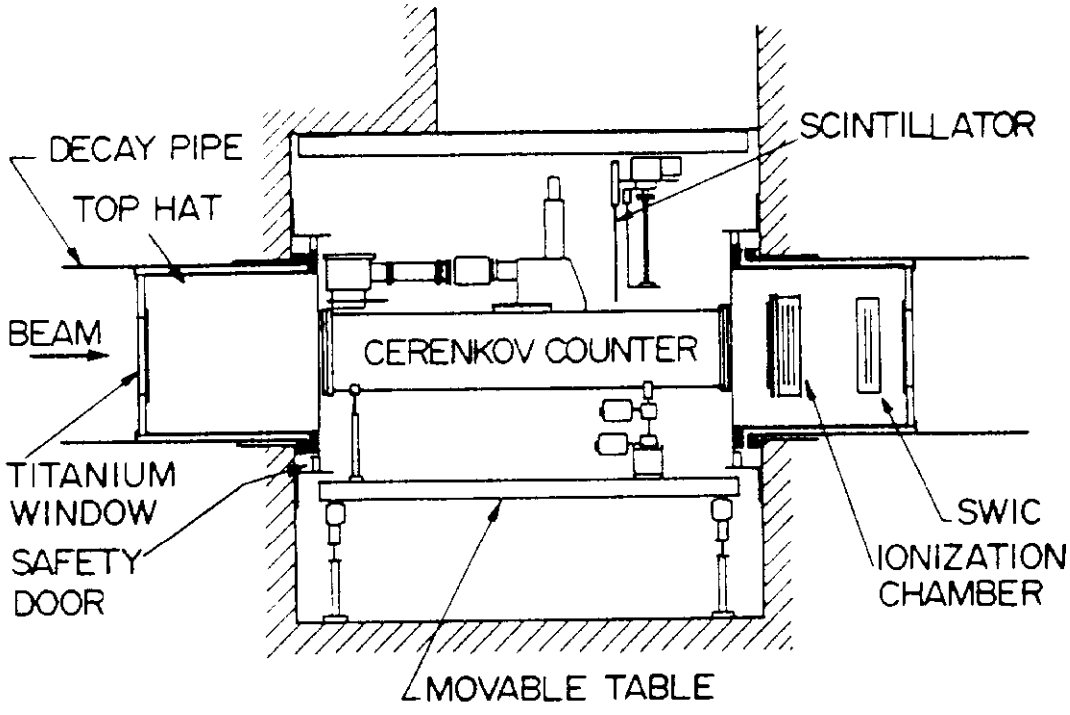

EXPANSION PORT
SIDE VIEW

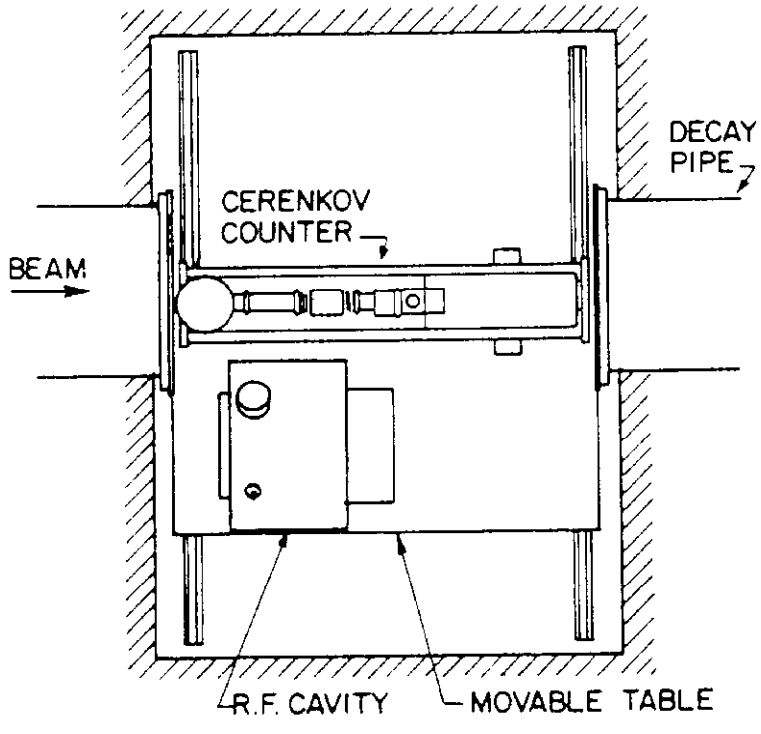

EXPANSION PORT
PLAN VIEW

Figure 4

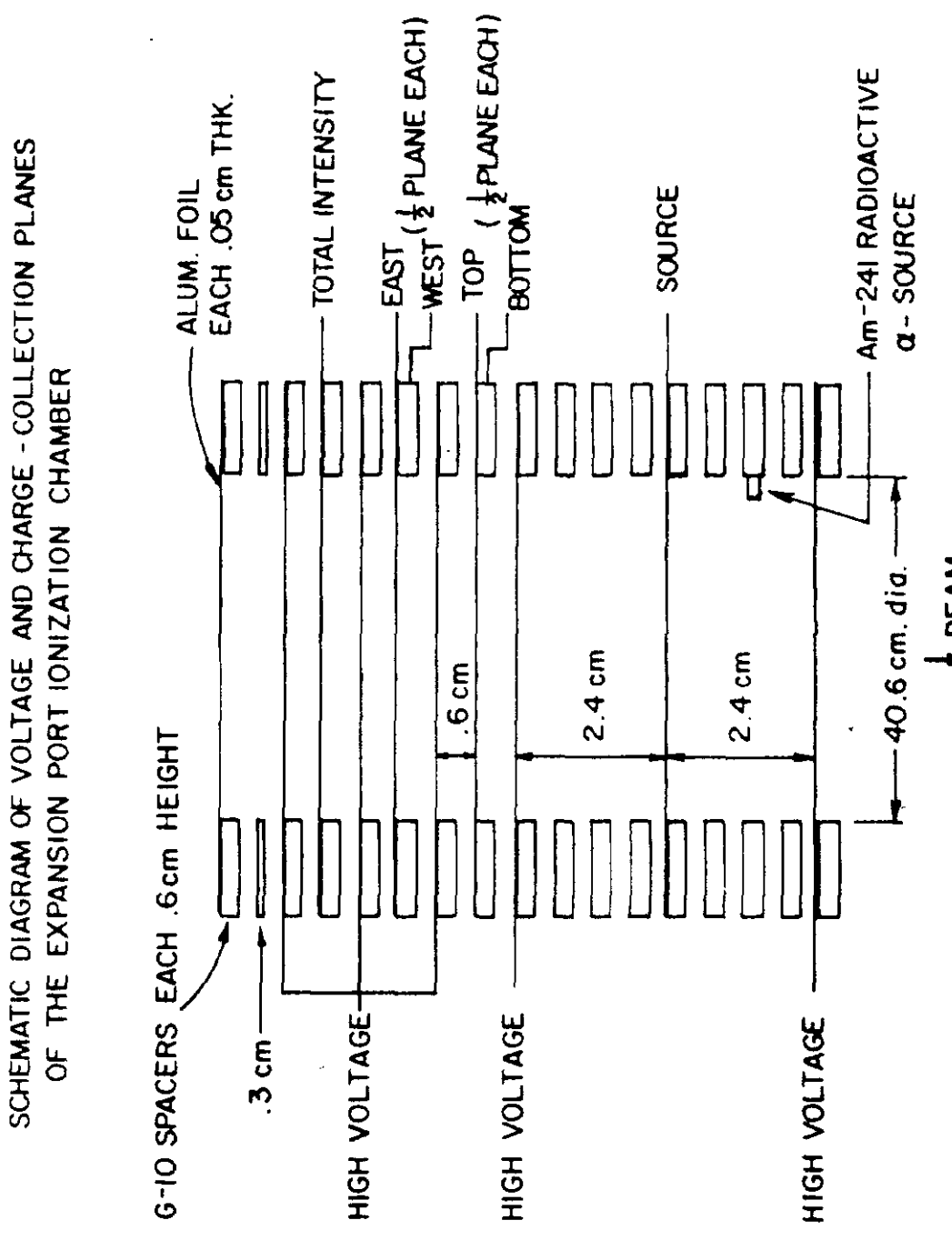
SCHEMATIC DIAGRAM OF VOLTAGE AND CHARGE - COLLECTION PLANES
OF THE EXPANSION PORT IONIZATION CHAMBER
G-10 SPACERS EACH .6cm HEIGHT
ALUM. FOIL
EACH .05 cm THK.
.3 cm
TOTAL INTENSITY
HIGH VOLTAGE
EAST
WEST (½ PLANE EACH)
.6 cm
TOP
BOTTOM (½ PLANE EACH)
HIGH VOLTAGE
2.4 cm
SOURCE
2.4 cm
HIGH VOLTAGE
Am-241 RADIOACTIVE
α - SOURCE
40.6 cm. dia.
BEAM

Figure 5

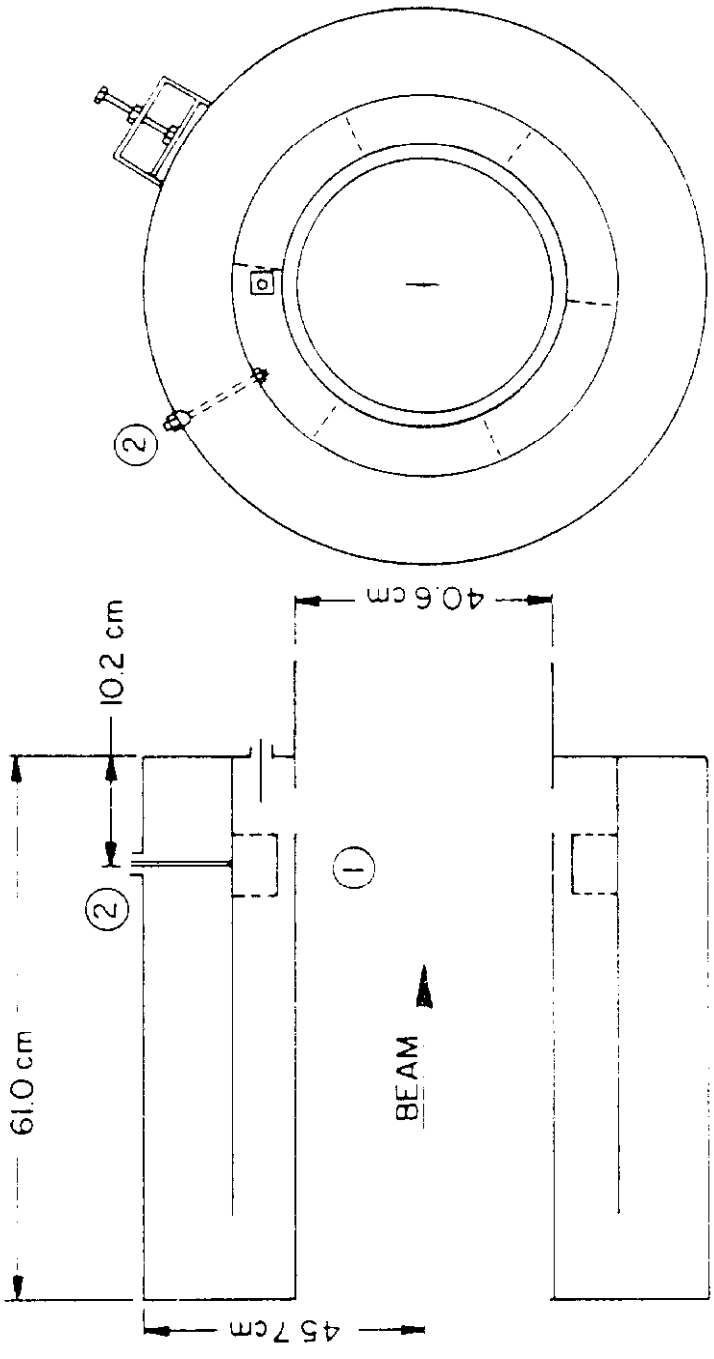

Figure 6

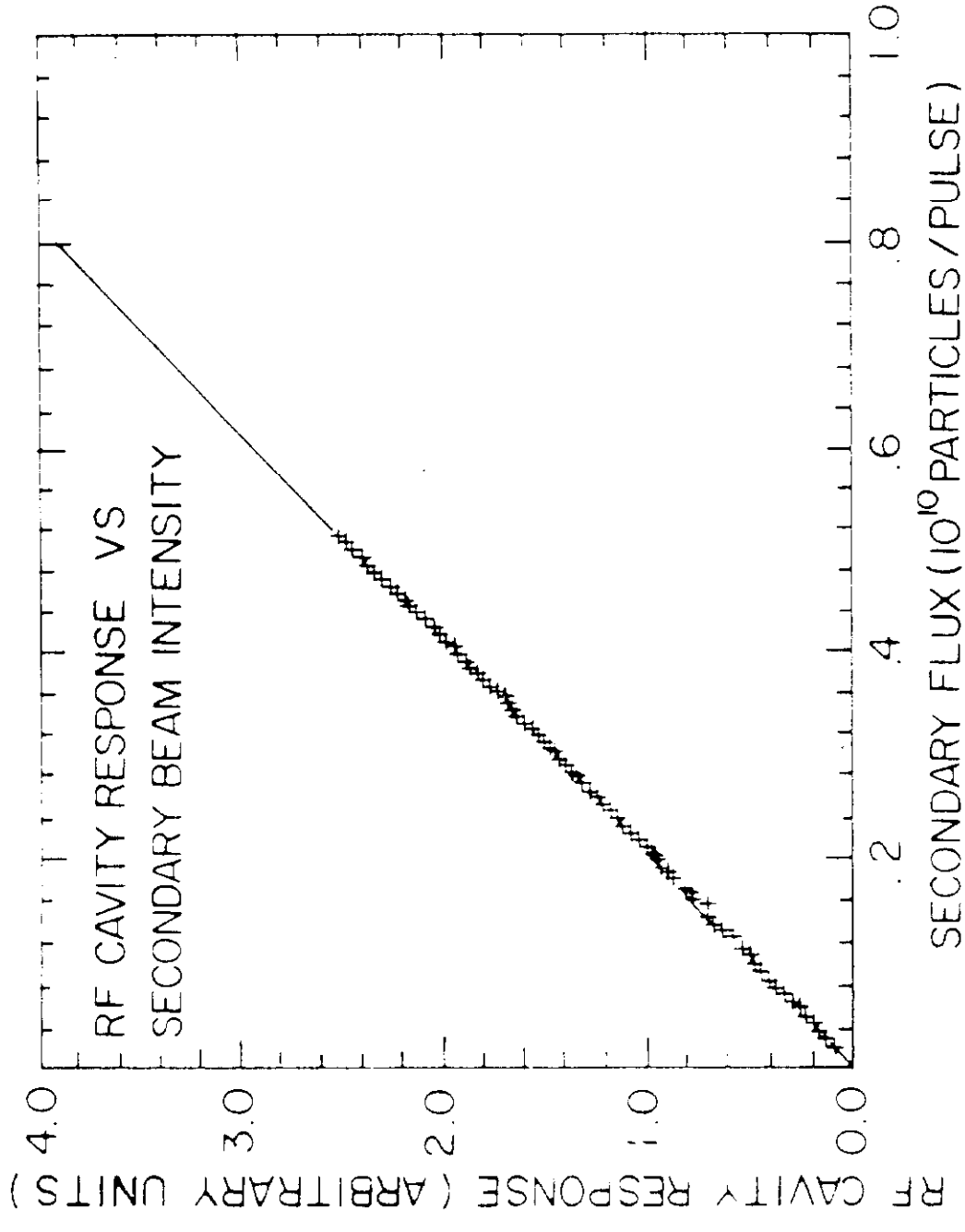
RF CAVITY RESPONSE VS
SECONDARY BEAM INTENSITY
RF CAVITY RESPONSE (ARBITRARY UNITS)
SECONDARY FLUX (10^10 PARTICLES/PULSE)
0.0
1.0
2.0
3.0
4.0
.2
.4
.6
.8
1.0

Figure 7

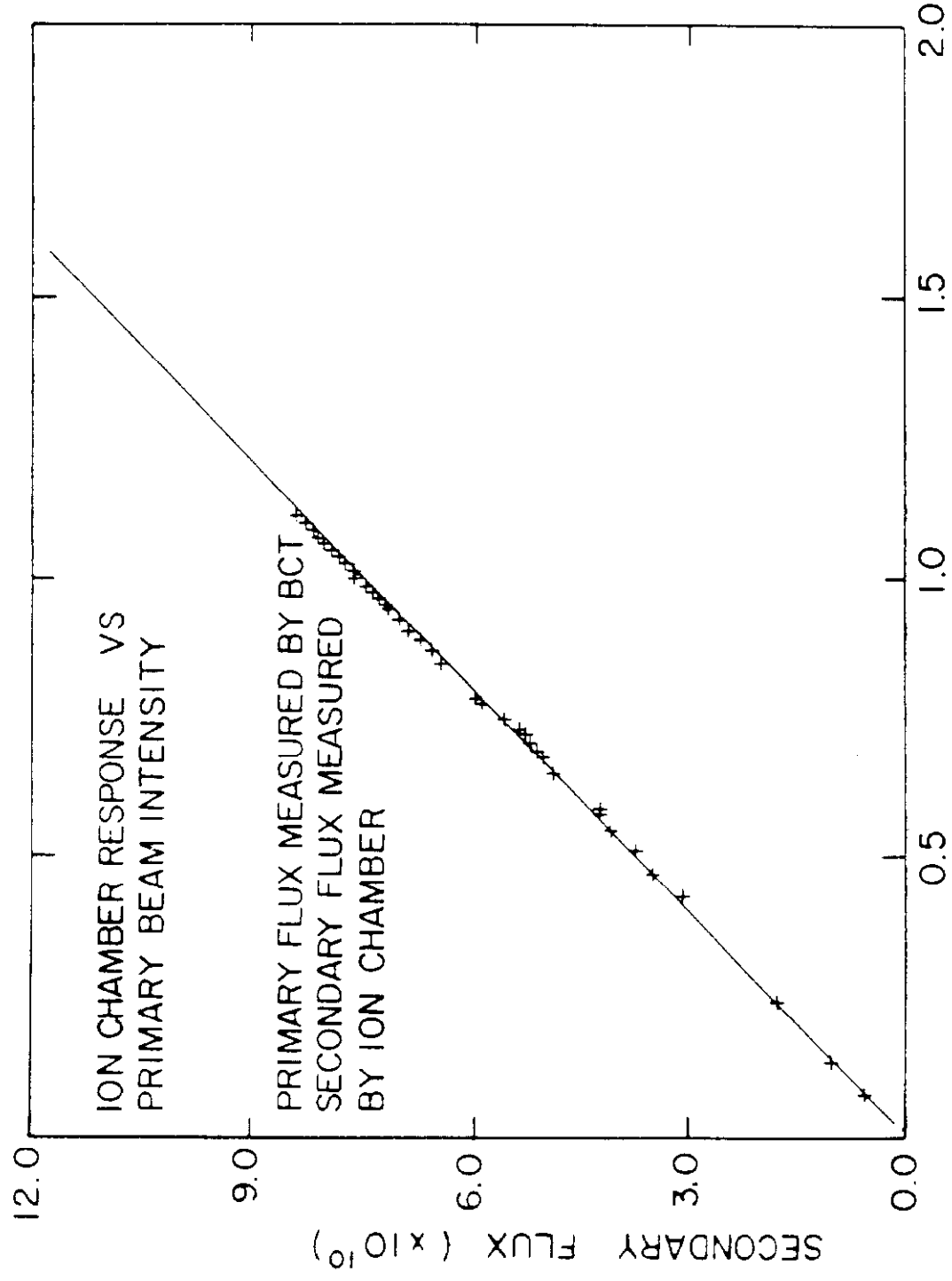
ION CHAMBER RESPONSE VS
PRIMARY BEAM INTENSITY
PRIMARY FLUX MEASURED BY BCT
SECONDARY FLUX MEASURED
BY ION CHAMBER
SECONDARY FLUX (x 10^10)
INCIDENT PROTON BEAM FLUX (x 10^13)
12.0
9.0
6.0
3.0
0.0
0.5
1.0
1.5
2.0

Figure 8

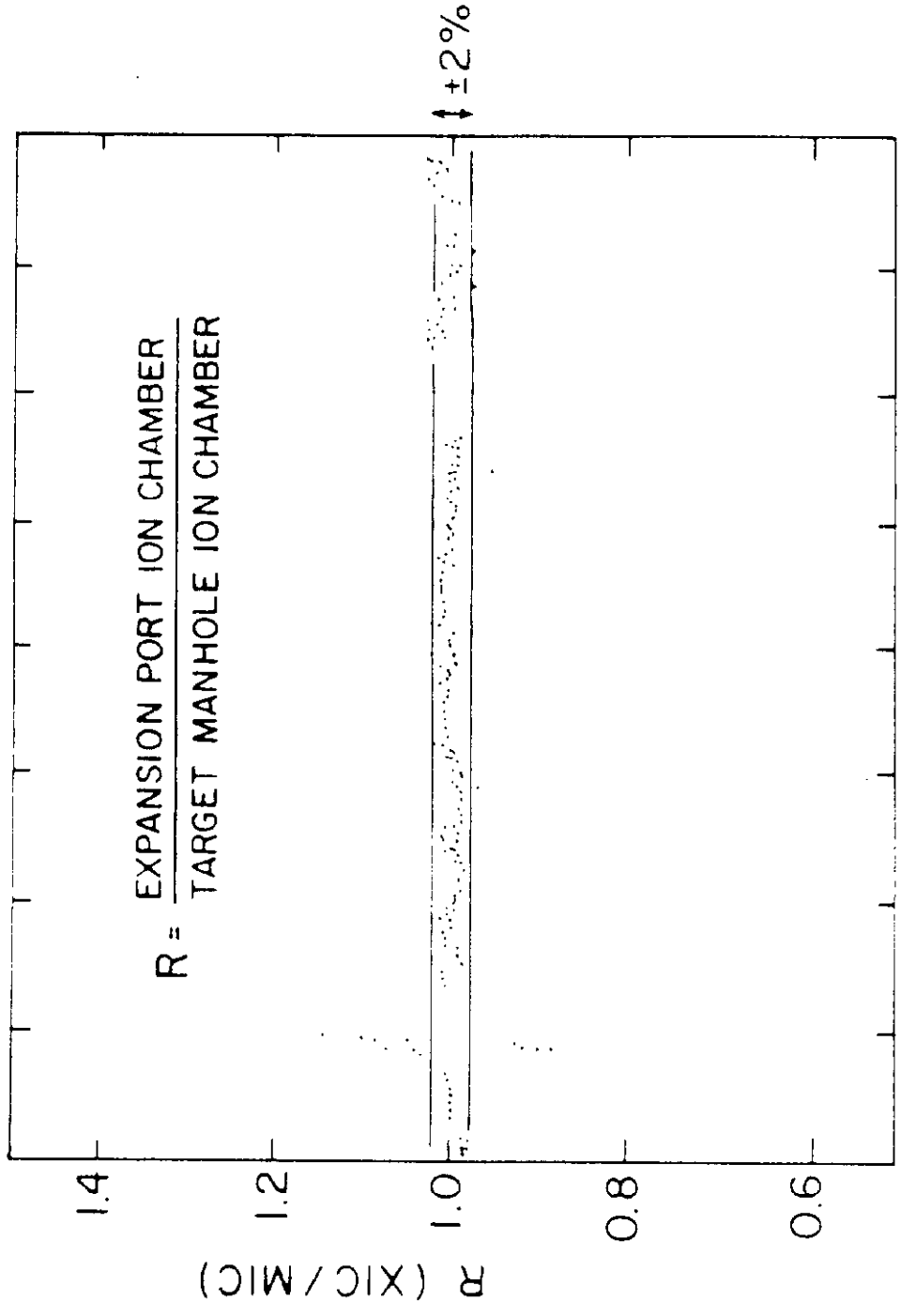
R = EXPANSION PORT ION CHAMBER / TARGET MANHOLE ION CHAMBER
±2%
R (XIC/MIC)
1.4
1.2
1.0
0.8
0.6
1400
1600
1800
2000
RUN NUMBER

Figure 9

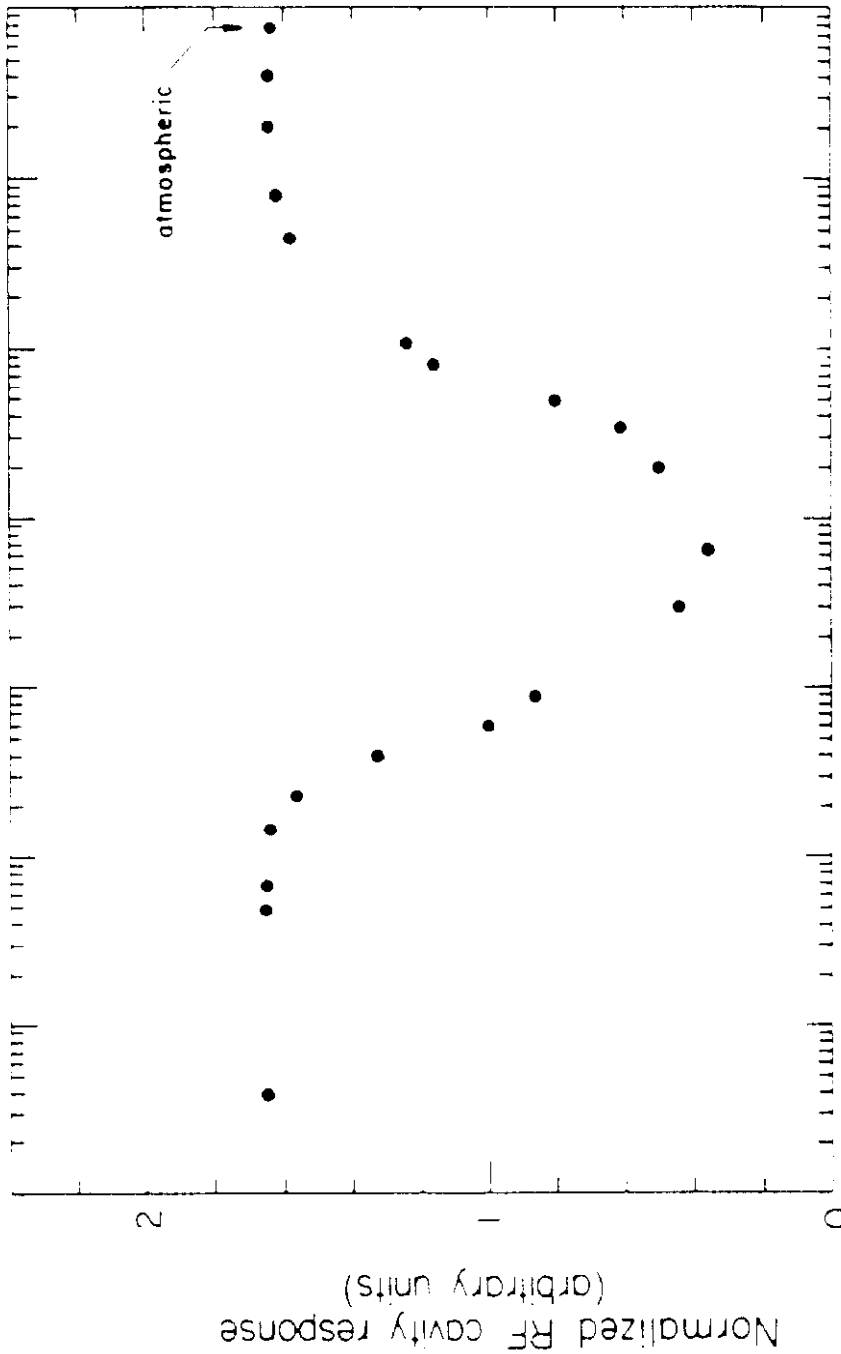
atmospheric
Normalized RF cavity response
(arbitrary units)
0
1
2
.001
.01
.1
1
10
100
Pressure (mm Hg)

Figure 10

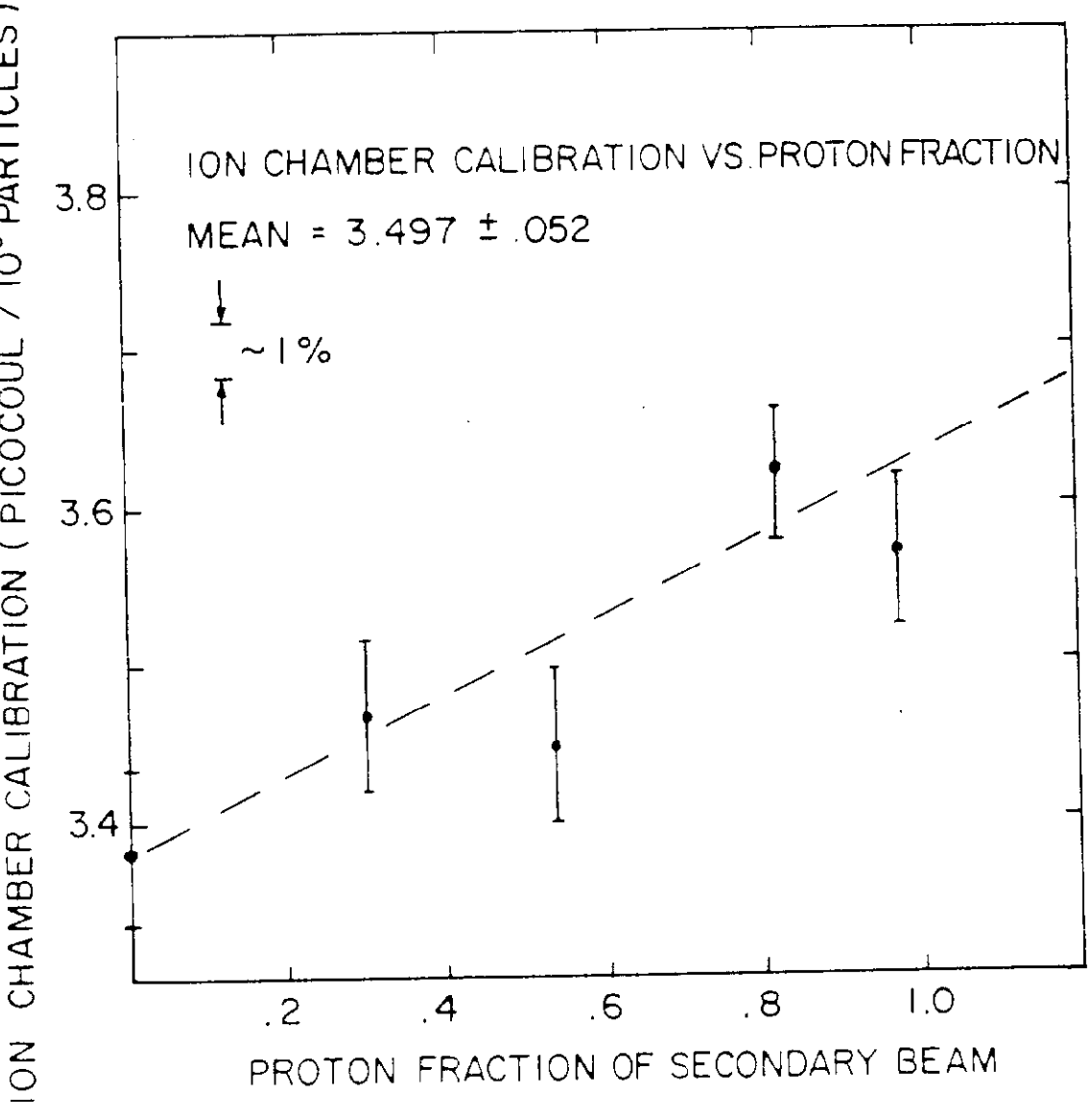
ION CHAMBER CALIBRATION VS. PROTON FRACTION
MEAN = 3.497 ± .052
~1%
ION CHAMBER CALIBRATION (PICOCOUL / 10^6 PARTICLES)
3.8
3.6
3.4
.2
.4
.6
.8
1.0
PROTON FRACTION OF SECONDARY BEAM

Figure 11

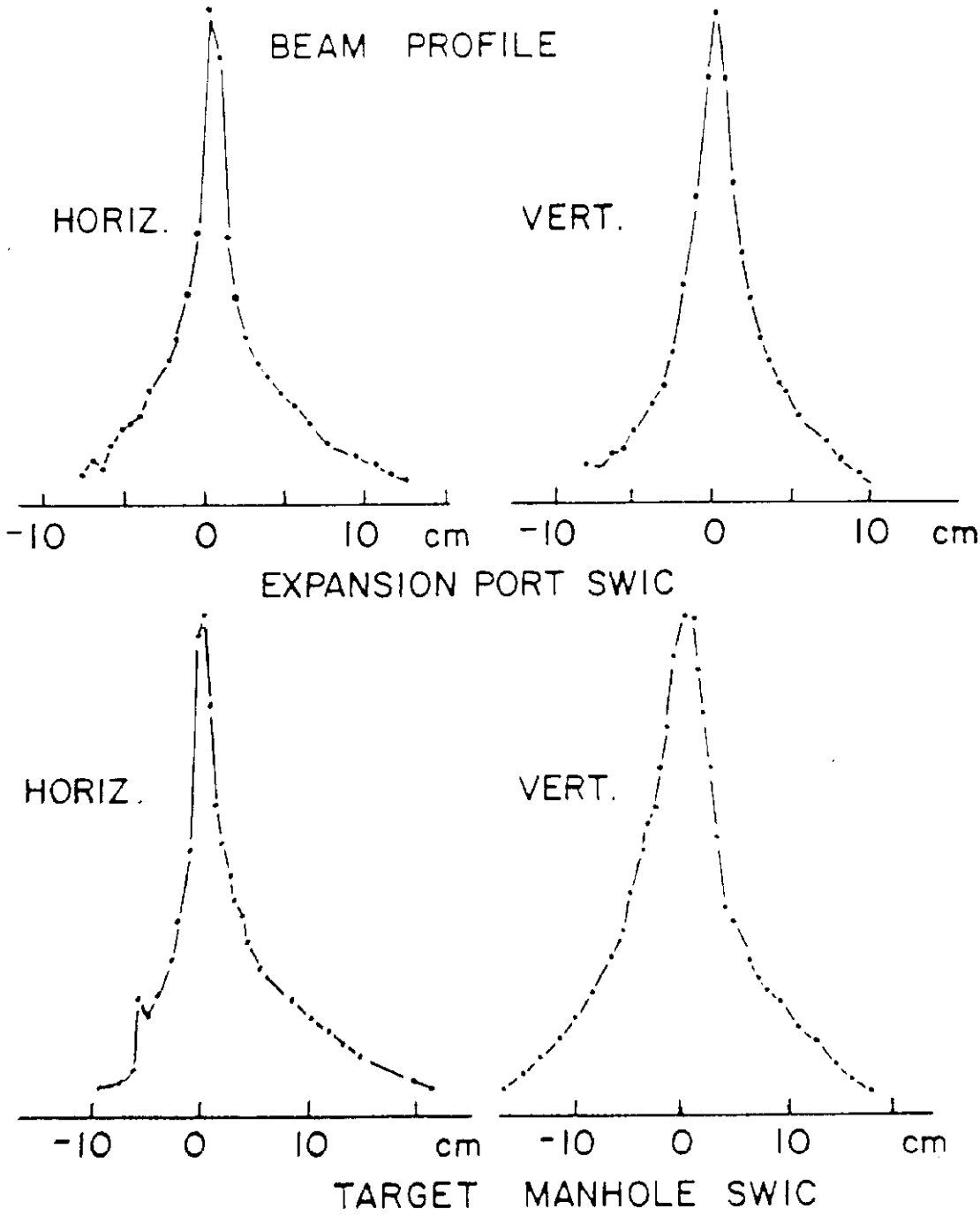
BEAM PROFILE
HORIZ.
VERT.
-10
0
10
cm
EXPANSION PORT SWIC
HORIZ.
VERT.
TARGET MANHOLE SWIC

Figure 12

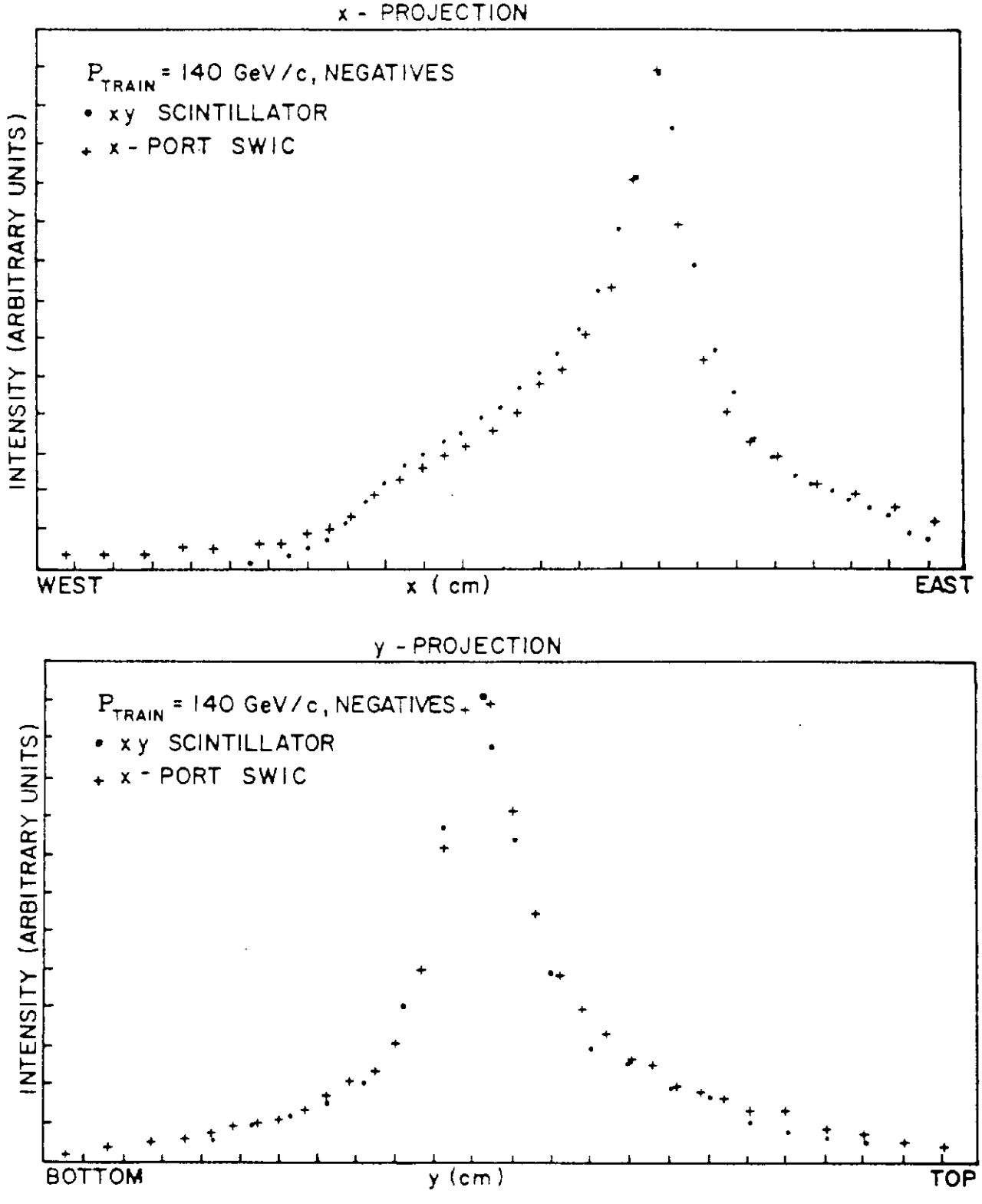
x - PROJECTION
P_{TRAIN} = 140 GeV/c, NEGATIVES
• xy SCINTILLATOR
+ x - PORT SWIC
INTENSITY (ARBITRARY UNITS)
WEST
x (cm)
EAST
y - PROJECTION
P_{TRAIN} = 140 GeV/c, NEGATIVES
• xy SCINTILLATOR
+ x - PORT SWIC
INTENSITY (ARBITRARY UNITS)
BOTTOM
y (cm)
TOP

Figure 13

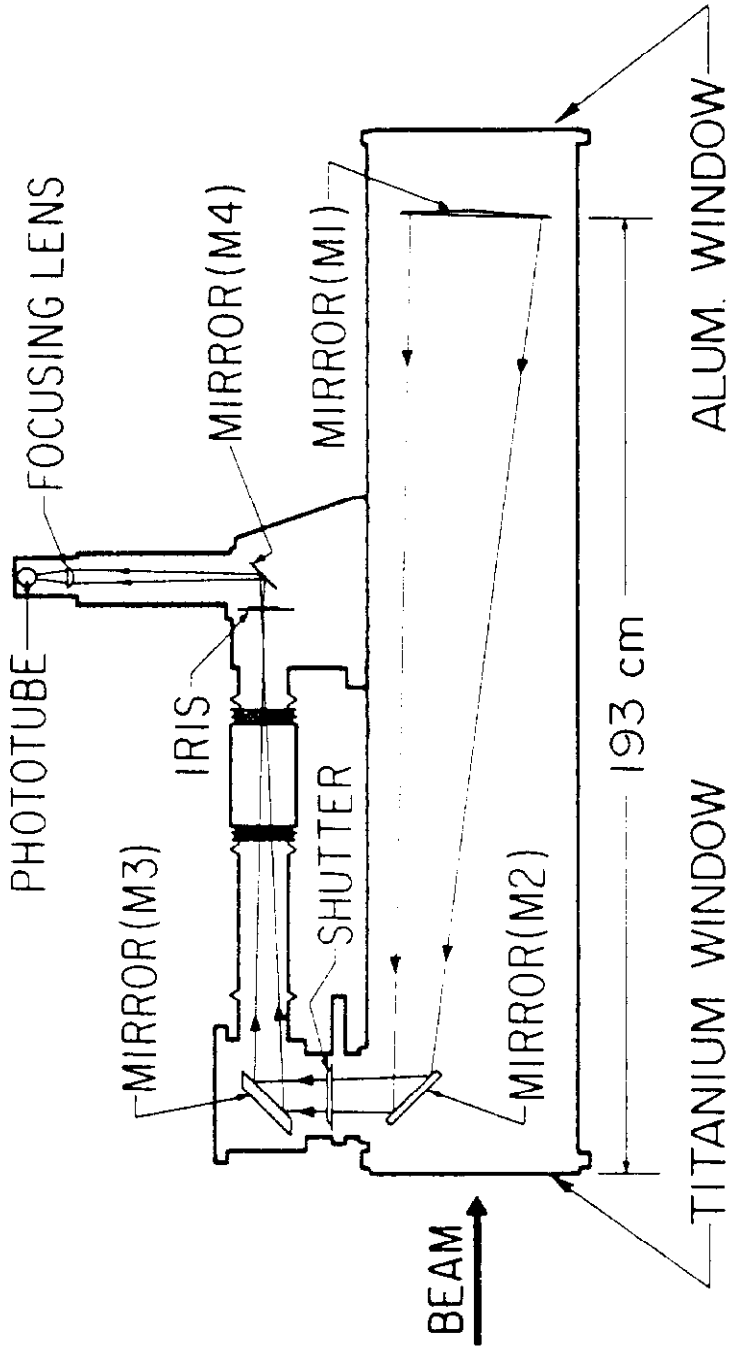
PHOTOTUBE
FOCUSING LENS
MIRROR(M4)
MIRROR(MI)
ALUM. WINDOW
IRIS
SHUTTER
MIRROR(M3)
MIRROR(M2)
193 cm
BEAM
TITANIUM WINDOW

Figure 14

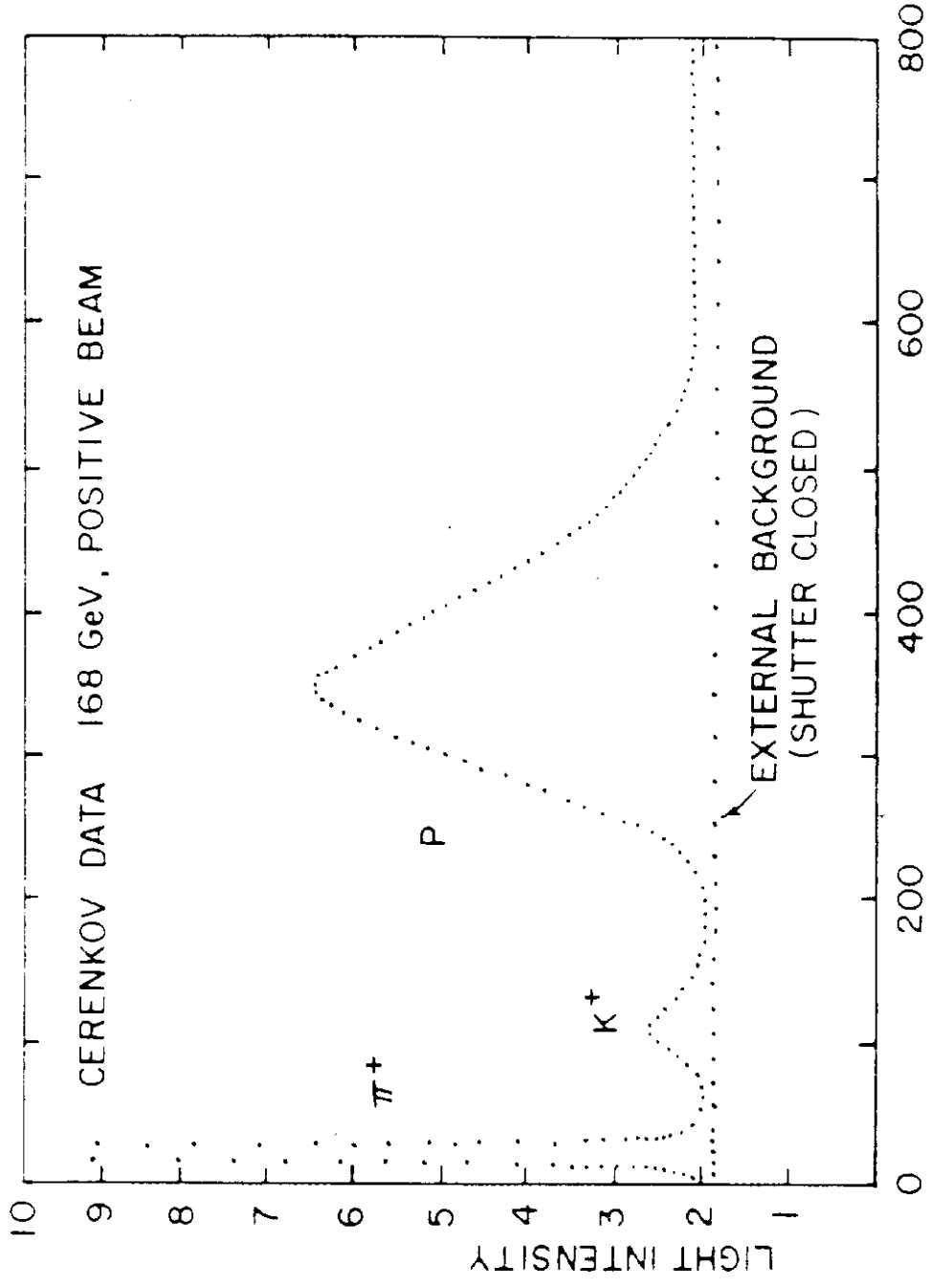
CERENKOV DATA 168 GeV, POSITIVE BEAM
LIGHT INTENSITY
PRESSURE (mm Hg)
EXTERNAL BACKGROUND
(SHUTTER CLOSED)
π^+
K^+
P
0
200
400
600
800
1
2
3
4
5
6
7
8
9
10

Figure 15

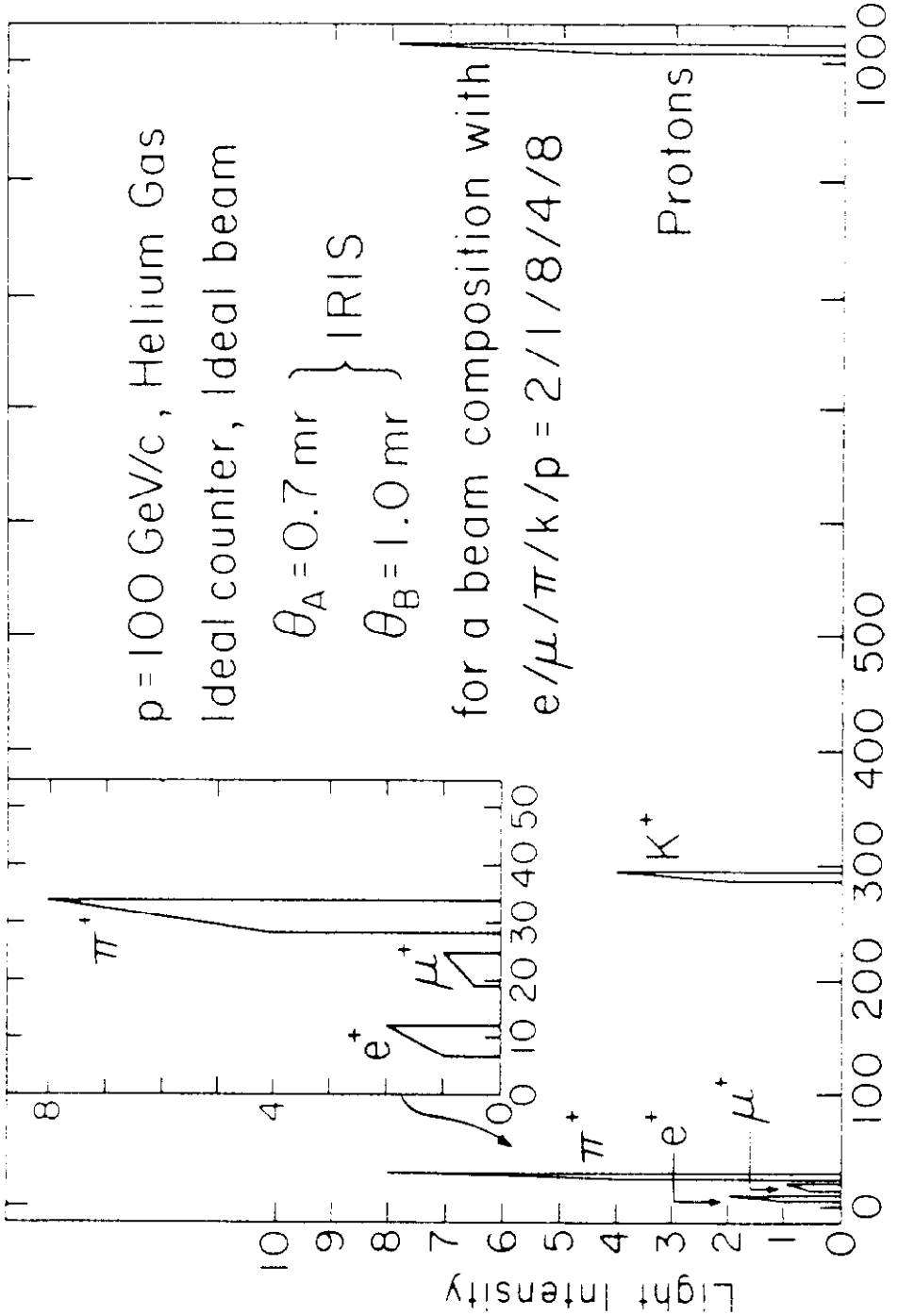
p = 100 GeV/c, Helium Gas
Ideal counter, Ideal beam
θ_A = 0.7 mr
θ_B = 1.0 mr
IRIS
for a beam composition with
e/μ/π/k/p = 2/1/8/4/8
Protons
Light Intensity
Pressure (mm Hg)
π^+
e^+
μ^+
K^+

Figure 16

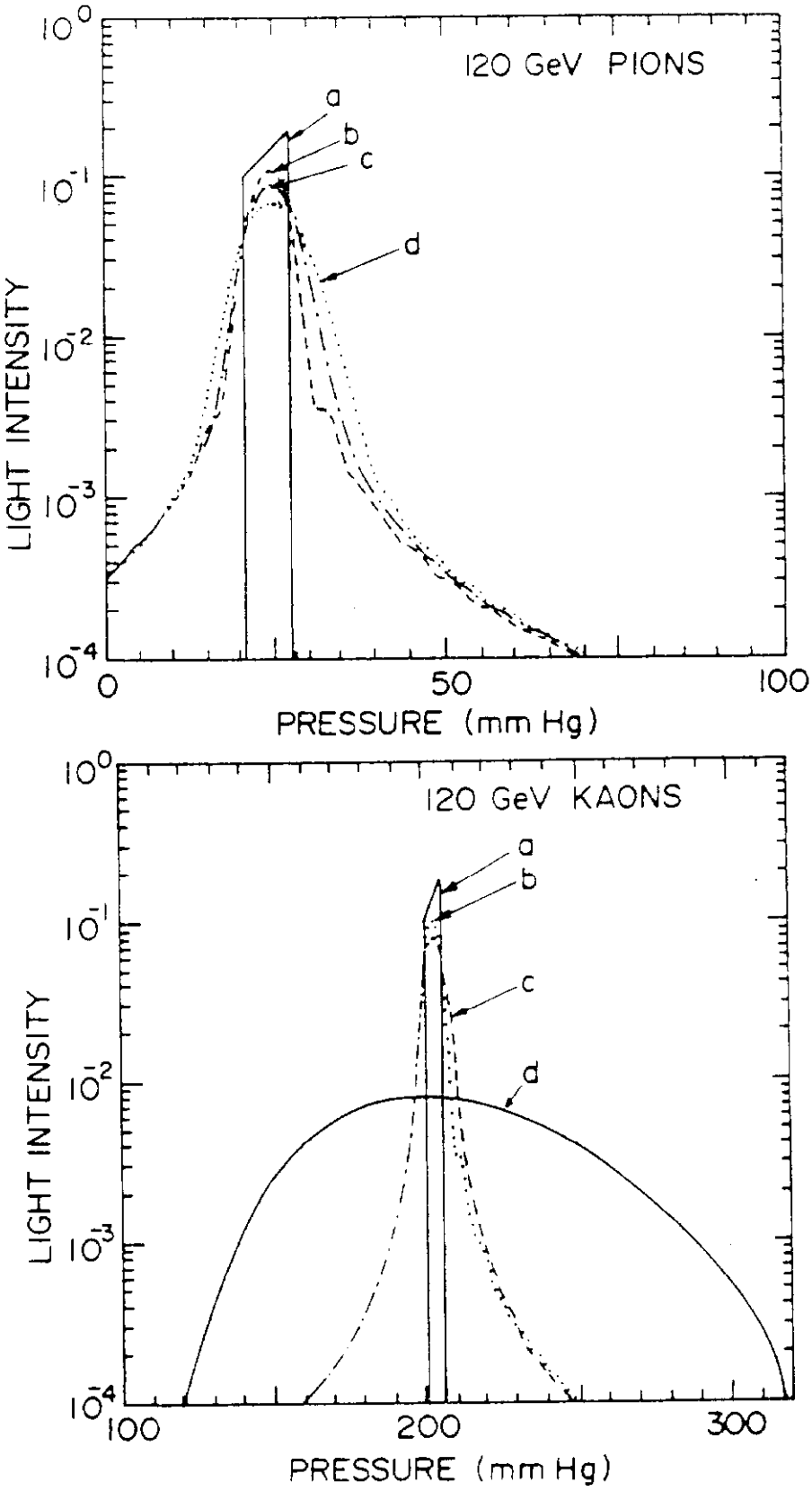
120 GeV PIONS
a
b
c
d
LIGHT INTENSITY
10^{0}
10^{-1}
10^{-2}
10^{-3}
10^{-4}
0
50
100
PRESSURE (mm Hg)
120 GeV KAONS
a
b
c
d
LIGHT INTENSITY
10^{0}
10^{-1}
10^{-2}
10^{-3}
10^{-4}
100
200
300
PRESSURE (mm Hg)

Figure 17

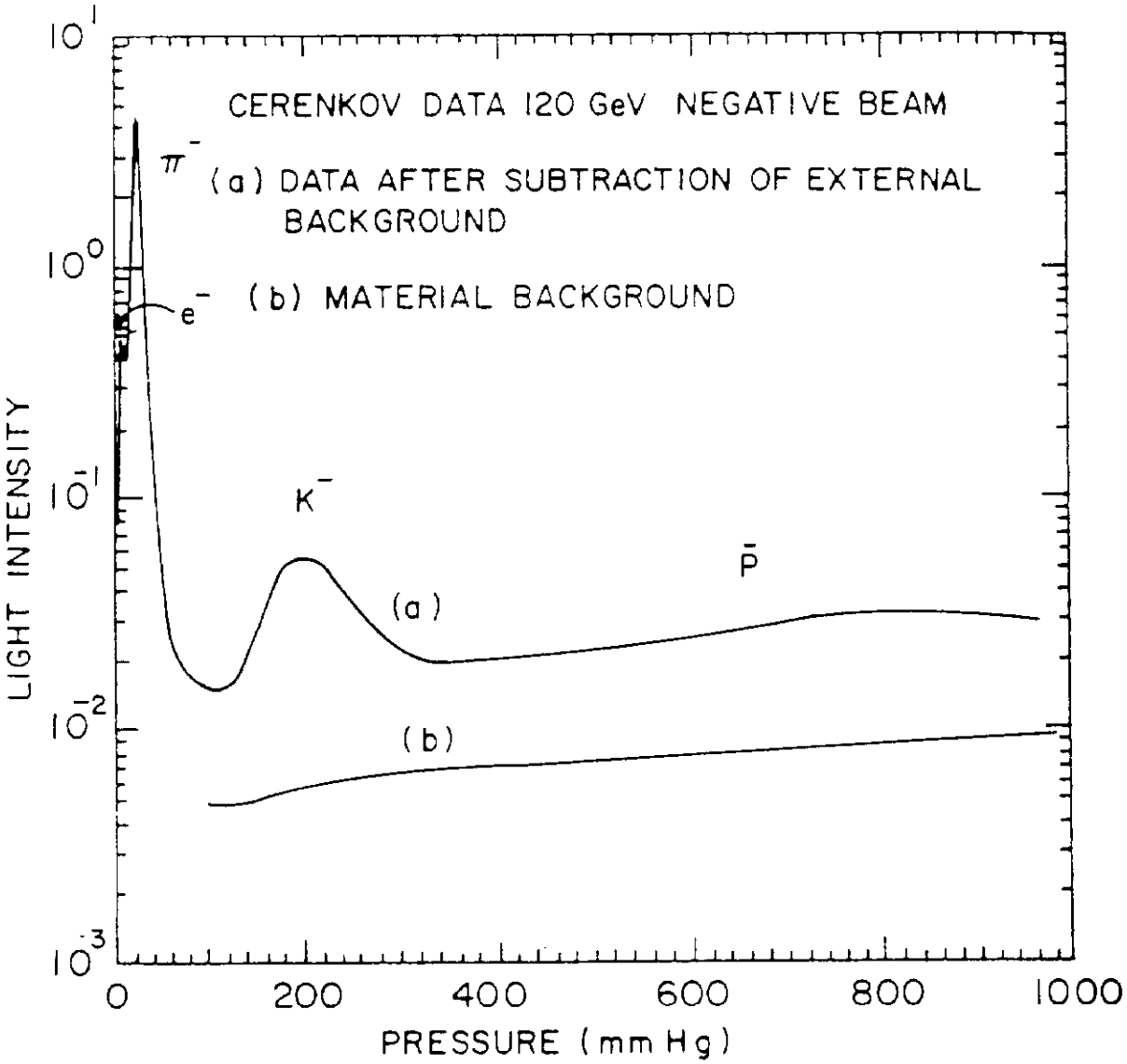
CERENKOV DATA 120 GeV NEGATIVE BEAM
(a) DATA AFTER SUBTRACTION OF EXTERNAL BACKGROUND
(b) MATERIAL BACKGROUND
π^-
e^-
K^-
$\bar{P}$
(a)
(b)
LIGHT INTENSITY
10^1
10^0
10^{-1}
10^{-2}
10^{-3}
0
200
400
600
800
1000
PRESSURE (mm Hg)

Figure 18

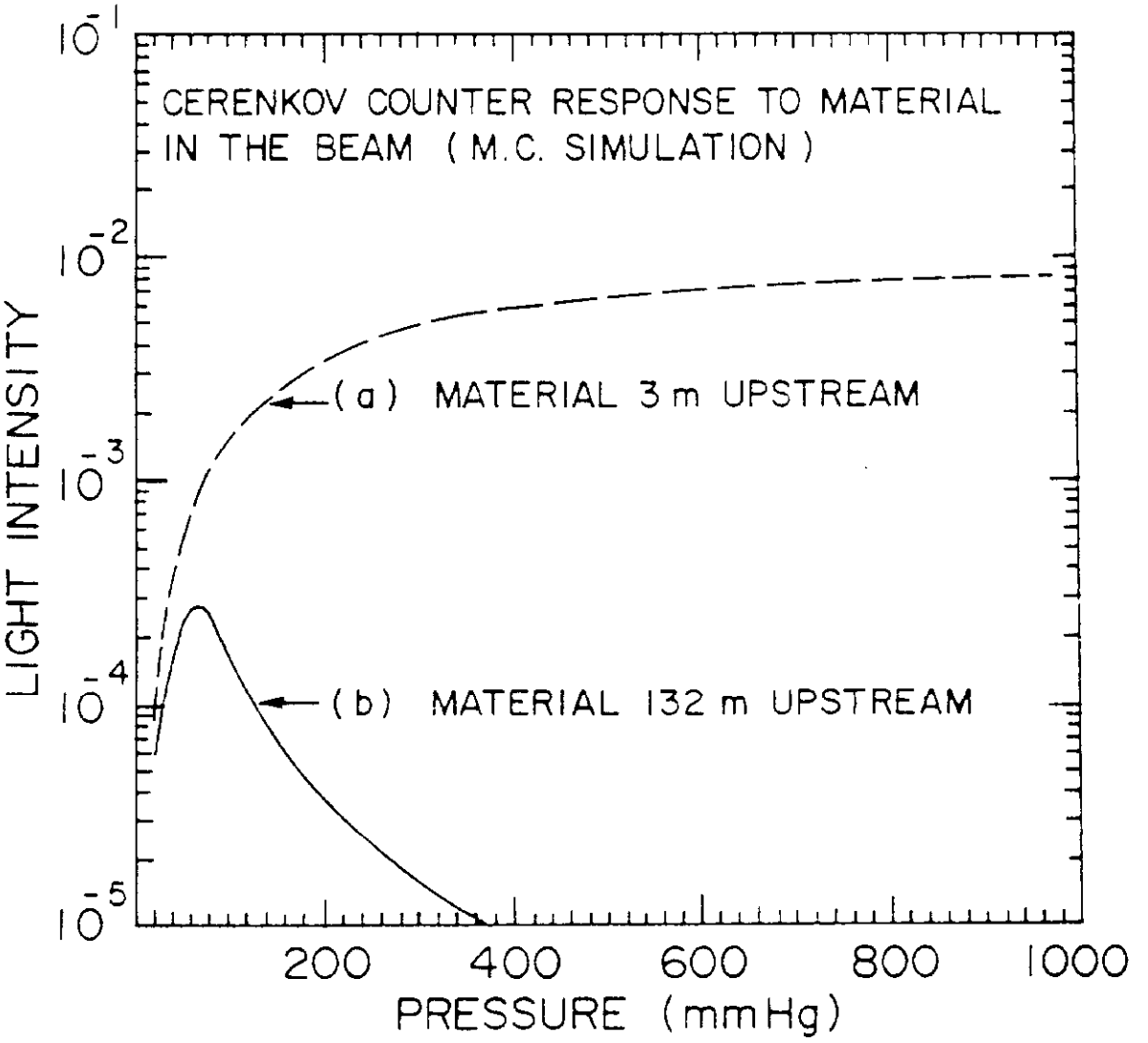
CERENKOV COUNTER RESPONSE TO MATERIAL
IN THE BEAM (M.C. SIMULATION)
LIGHT INTENSITY
10⁻¹
10⁻²
10⁻³
10⁻⁴
10⁻⁵
(a) MATERIAL 3 m UPSTREAM
(b) MATERIAL 132 m UPSTREAM
200
400
600
800
1000
PRESSURE (mmHg)

Figure 19

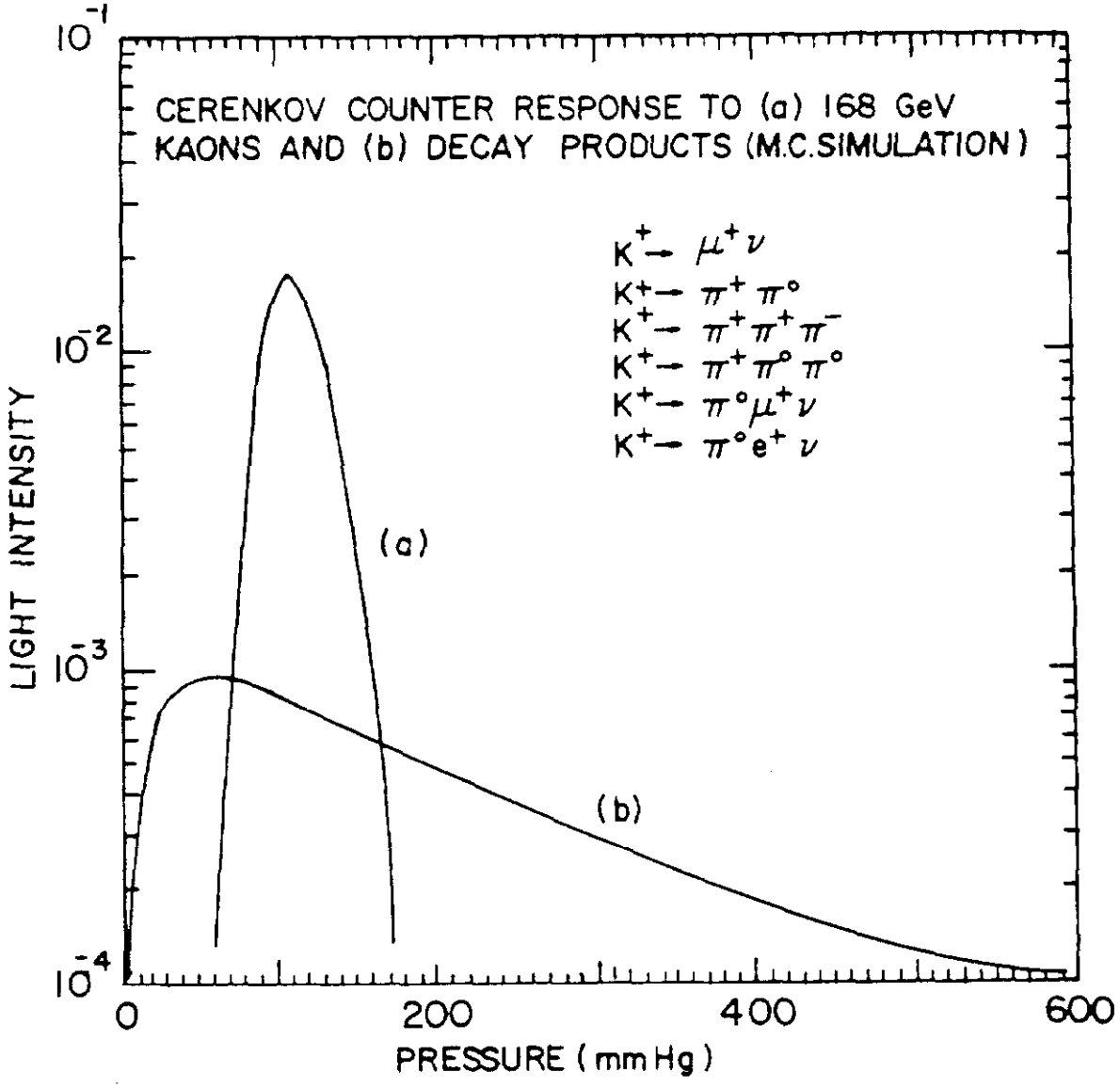
CERENKOV COUNTER RESPONSE TO (a) 168 GeV
KAONS AND (b) DECAY PRODUCTS (M.C.SIMULATION)
$K^+ \to \mu^+ \nu$
$K^+ \to \pi^+ \pi^\circ$
$K^+ \to \pi^+ \pi^+ \pi^-$
$K^+ \to \pi^+ \pi^\circ \pi^\circ$
$K^+ \to \pi^\circ \mu^+ \nu$
$K^+ \to \pi^\circ e^+ \nu$
(a)
(b)
LIGHT INTENSITY
10^{-1}
10^{-2}
10^{-3}
10^{-4}
0
200
400
600
PRESSURE (mm Hg)

Figure 20

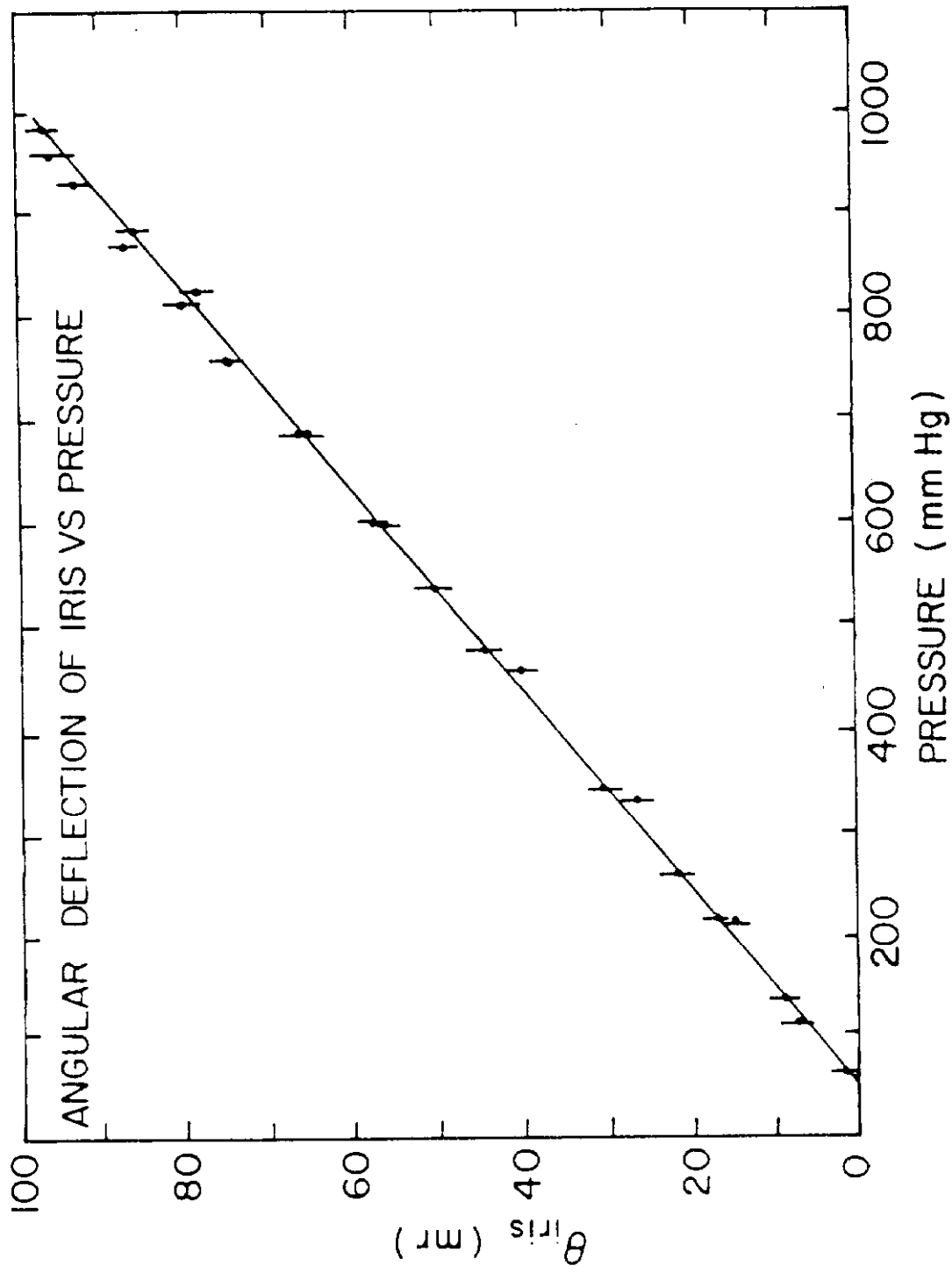
ANGULAR DEFLECTION OF IRIS VS PRESSURE
θ_{iris} (mr)
PRESSURE (mm Hg)
0
20
40
60
80
100
200
400
600
800
1000

Figure 21

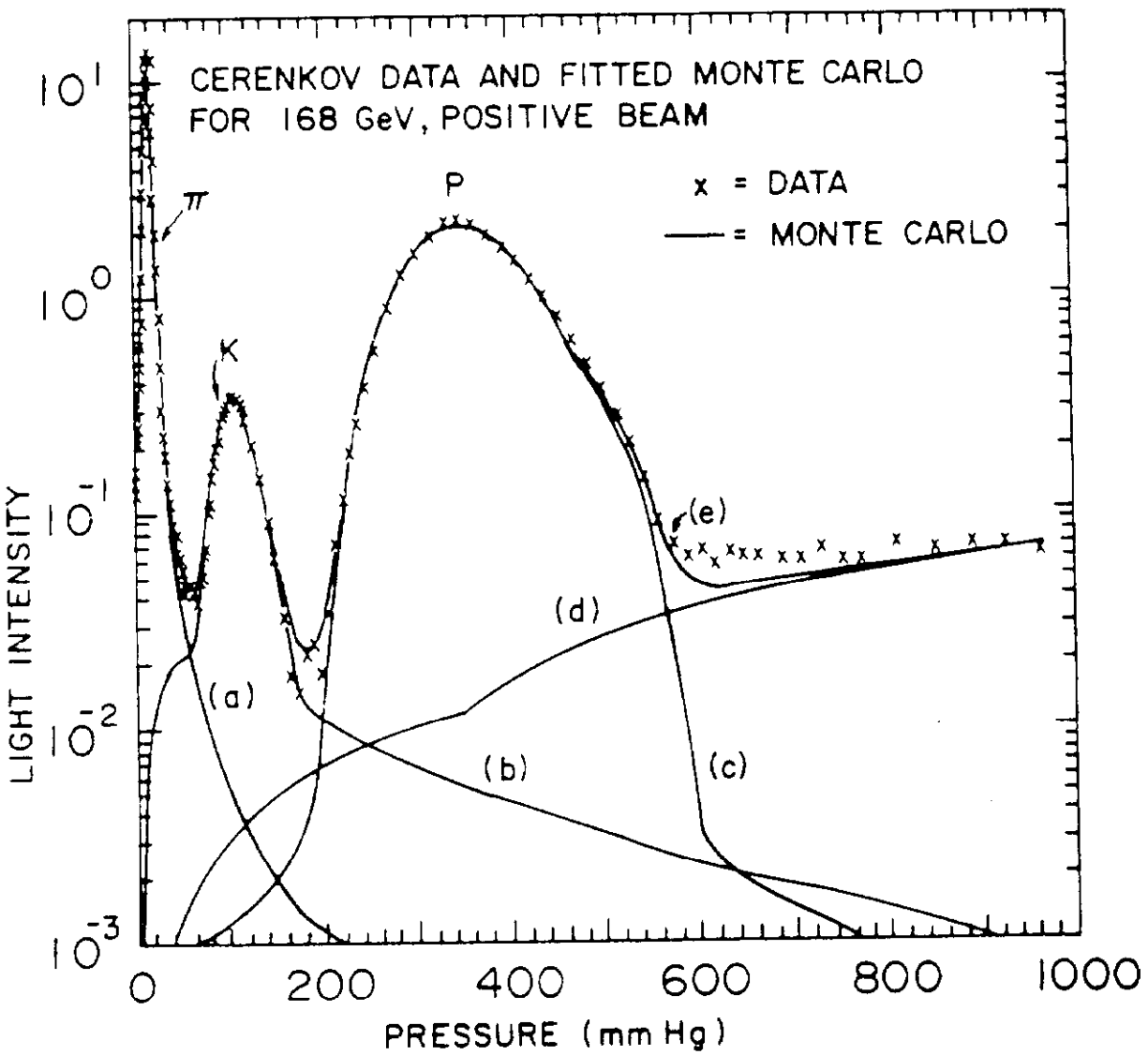
CERENKOV DATA AND FITTED MONTE CARLO
FOR 168 GeV, POSITIVE BEAM
x = DATA
= MONTE CARLO
π
K
P
(a)
(b)
(c)
(d)
(e)
LIGHT INTENSITY
PRESSURE (mm Hg)
0
200
400
600
800
1000

Figure 22

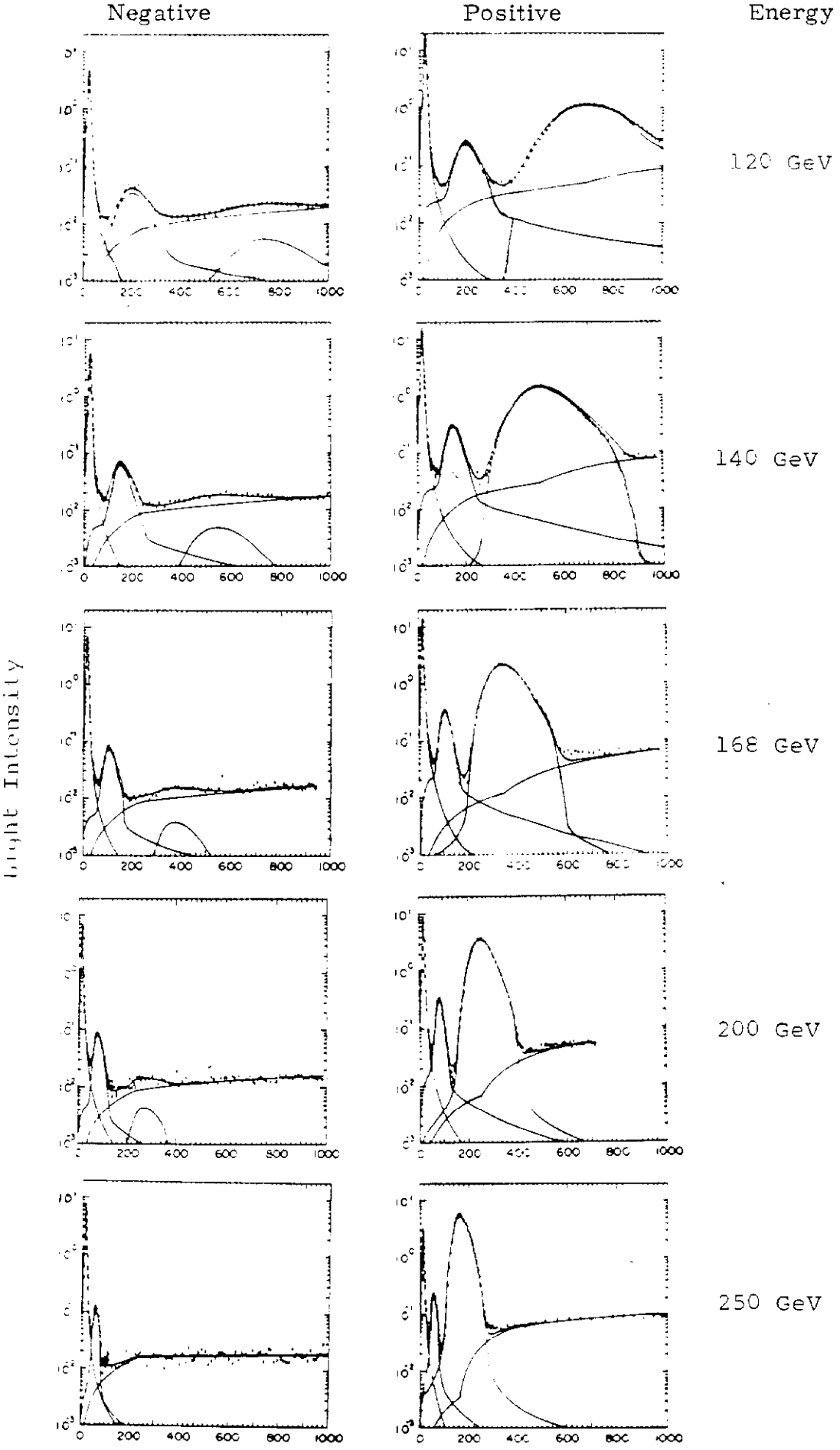
Negative
Positive
Energy
120 GeV
140 GeV
168 GeV
200 GeV
250 GeV
Light Intensity
Pressure (mm Hg)

Figure 23

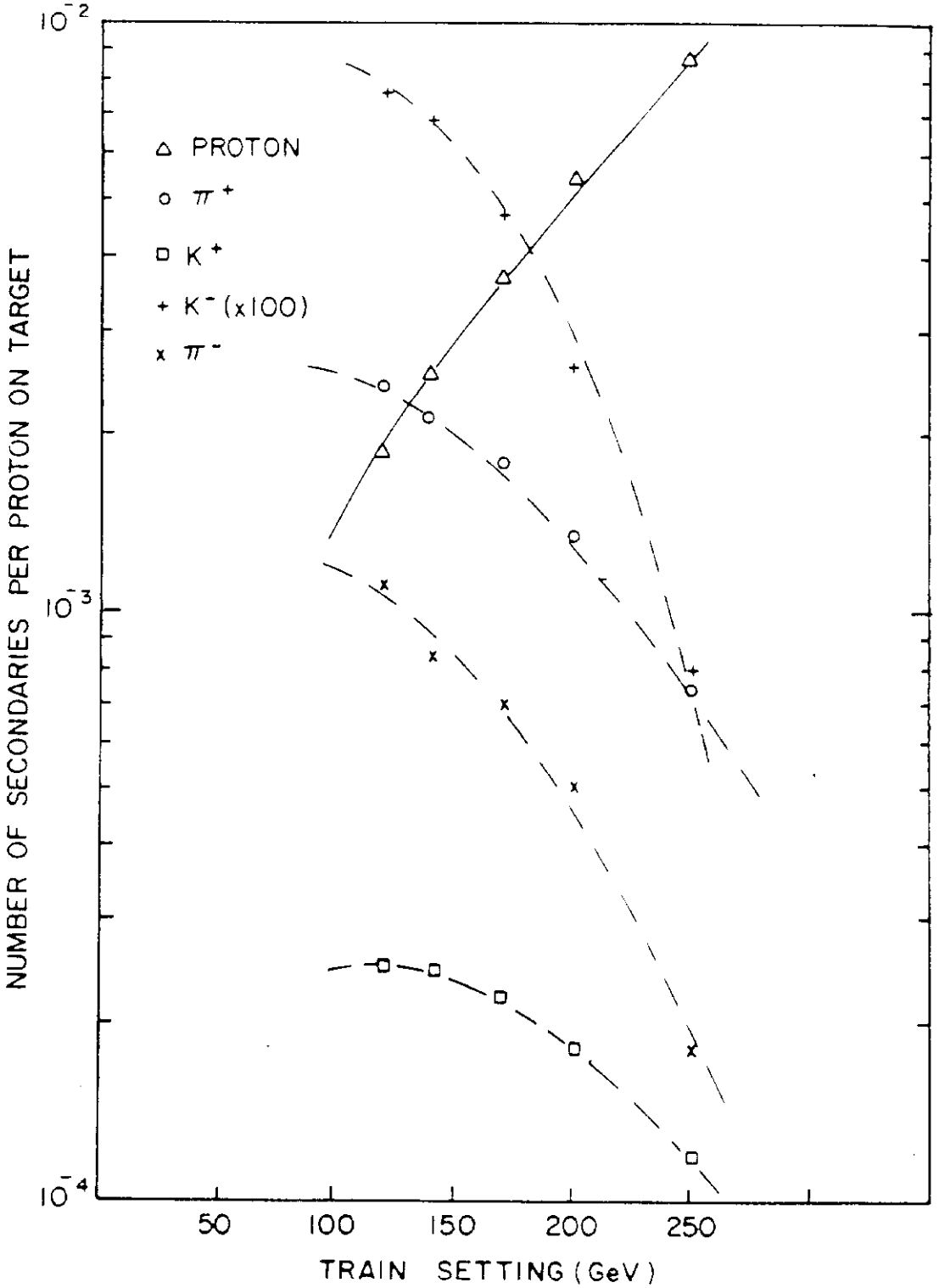
10^{-2}
10^{-3}
10^{-4}
Δ PROTON
o π^+
□ K^+
+ K^- (x100)
x π^-
NUMBER OF SECONDARIES PER PROTON ON TARGET
50
100
150
200
250
TRAIN SETTING (GeV)

Figure 24

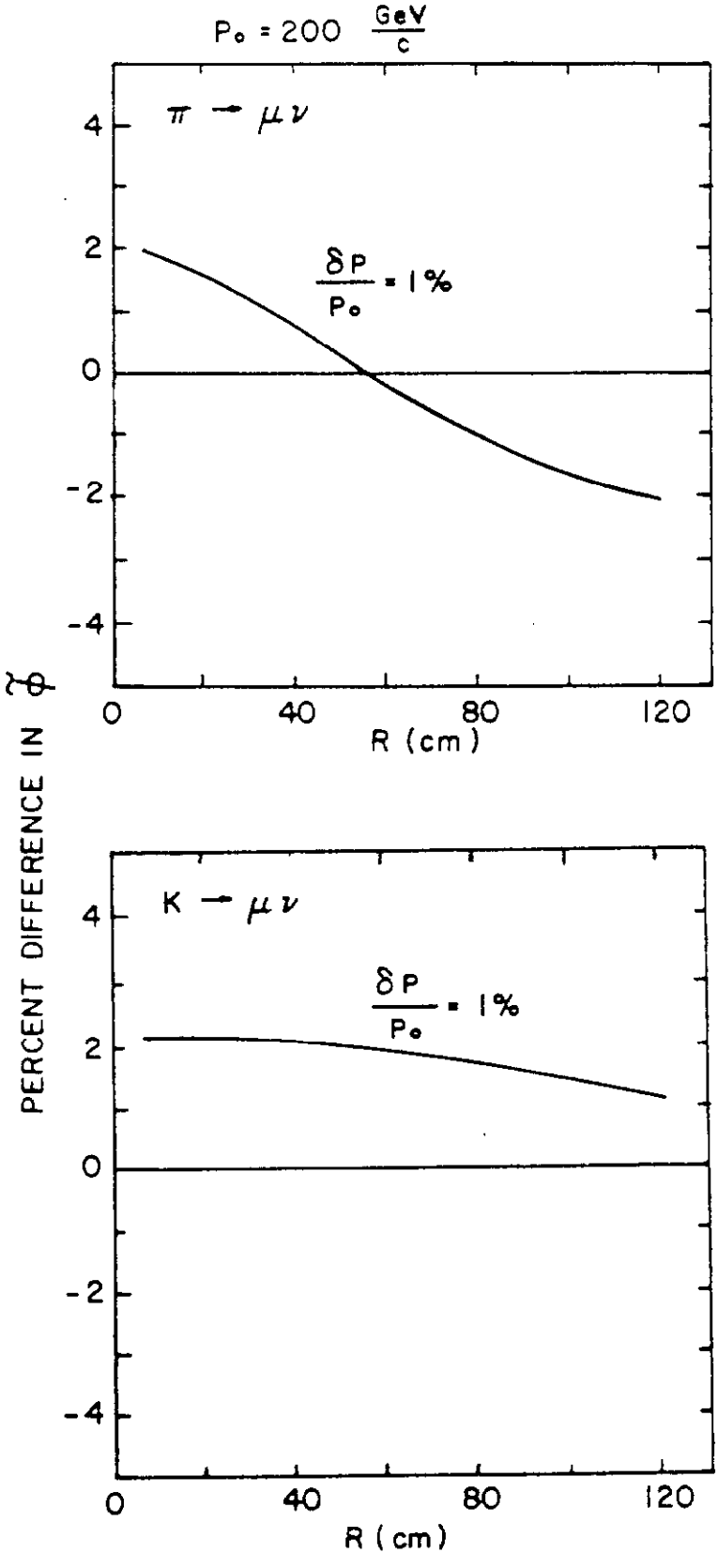
$P_o = 200 \frac{GeV}{c}$
$\pi \rightarrow \mu\nu$
$\frac{\delta P}{P_o} = 1\%$
$K \rightarrow \mu\nu$
$\frac{\delta P}{P_o} = 1\%$
PERCENT DIFFERENCE IN $\gamma\theta$
4
2
0
-2
-4
0
40
80
120
R (cm)

Figure 25

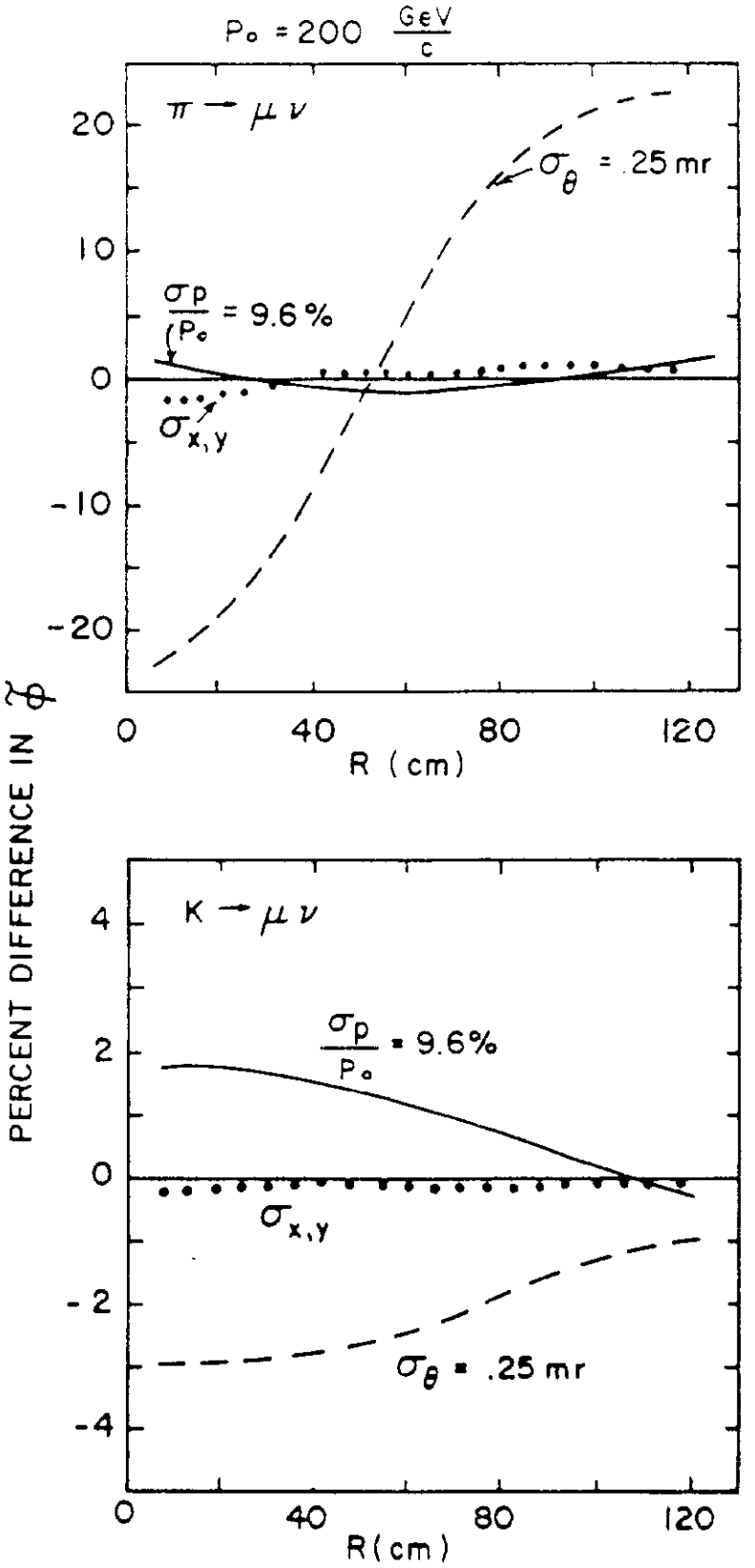
$P_o = 200 \frac{GeV}{c}$
$\pi \rightarrow \mu \nu$
$\sigma_\theta = .25$ mr
$\frac{\sigma p}{P_o} = 9.6\%$
$\sigma_{x,y}$
20
10
0
-10
-20
0
40
80
120
R (cm)
PERCENT DIFFERENCE IN ϕ
$K \rightarrow \mu \nu$
$\frac{\sigma p}{P_o} = 9.6\%$
$\sigma_{x,y}$
$\sigma_\theta = .25$ mr
4
2
0
-2
-4
0
40
80
120
R(cm)

Figure 26

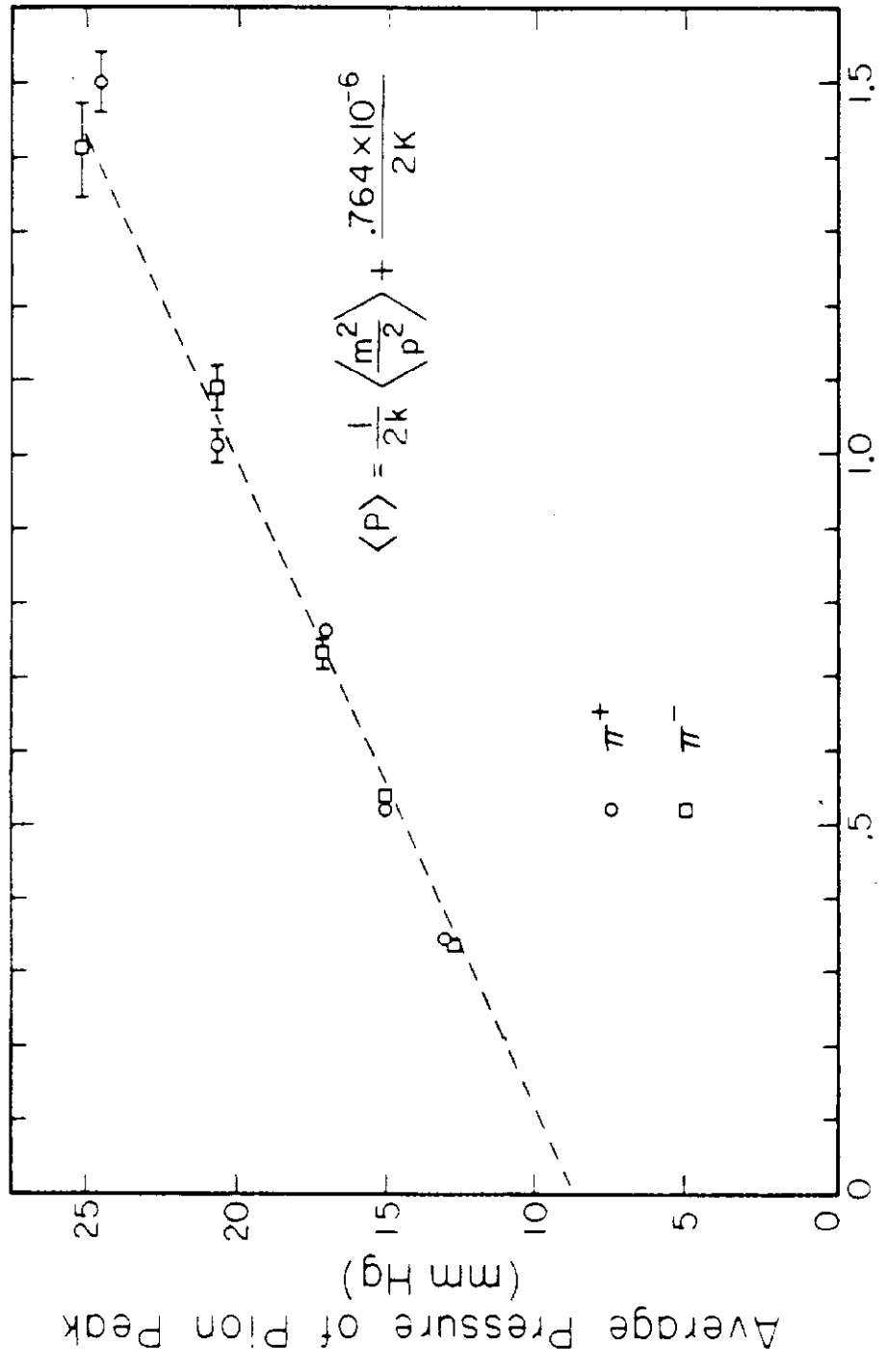
Average Pressure of Pion Peak
(mm Hg)
25
20
15
10
5
0
0
.5
1.0
1.5
$\frac{m^2}{p^2} \times 10^{-3}$
$\langle P \rangle = \frac{1}{2k} \left\langle \frac{m^2}{p^2} \right\rangle + \frac{.764 \times 10^{-6}}{2K}$
π^+
π^-

Figure 27

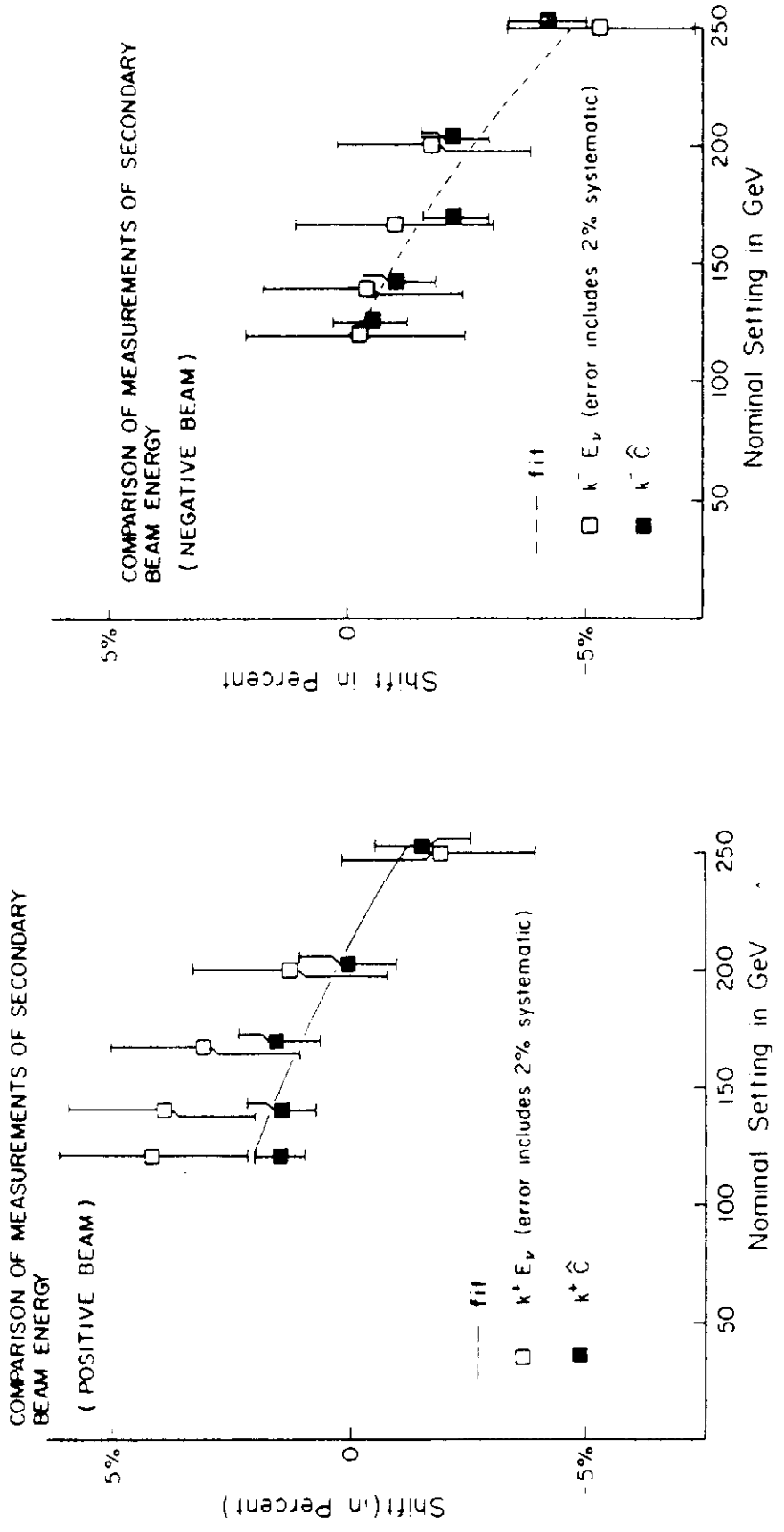
COMPARISON OF MEASUREMENTS OF SECONDARY BEAM ENERGY
(POSITIVE BEAM)
Shift (in Percent)
5%
0
-5%
50
100
150
200
250
Nominal Setting in GeV
fit
k⁺ E_ν (error includes 2% systematic)
k⁺ Ĉ
COMPARISON OF MEASUREMENTS OF SECONDARY BEAM ENERGY
(NEGATIVE BEAM)
Shift in Percent
k⁻ E_ν (error includes 2% systematic)
k⁻ Ĉ

Figure 28

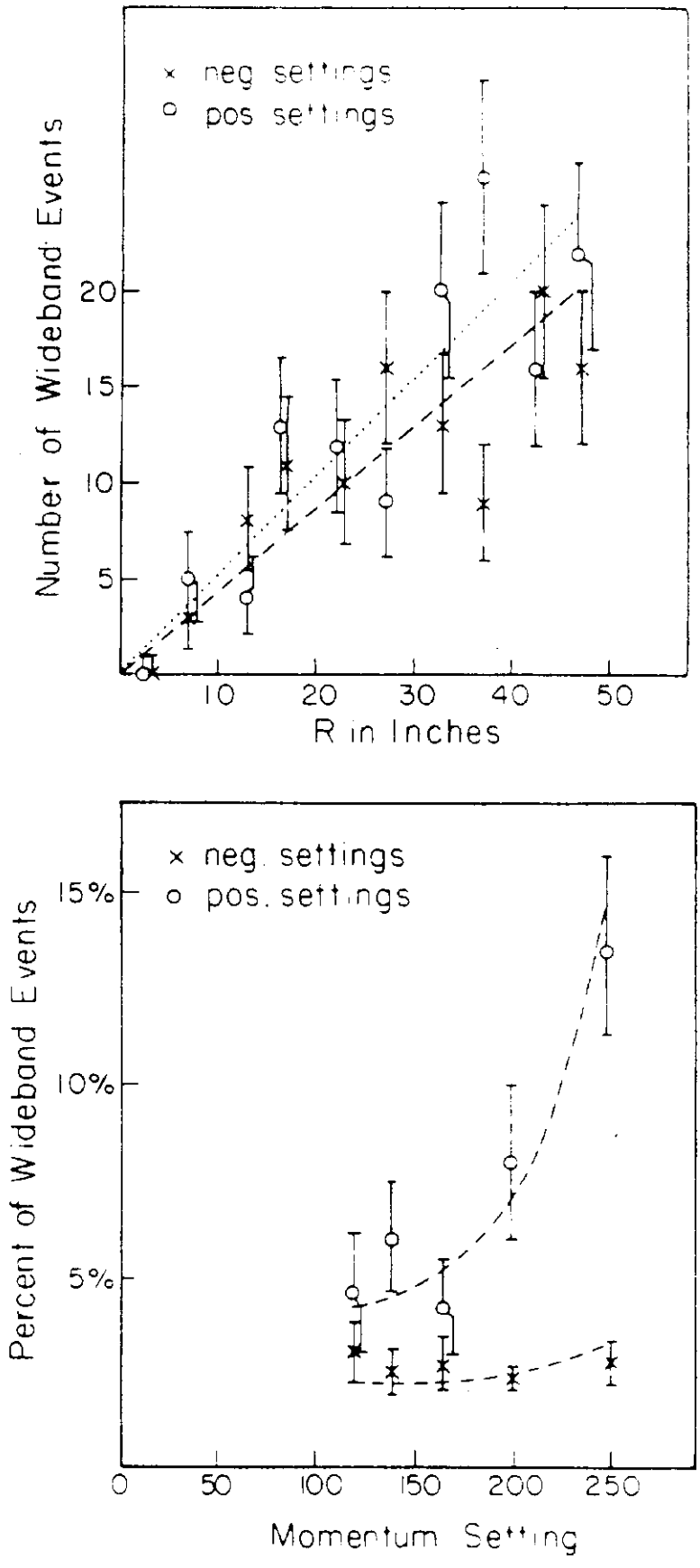
× neg settings
o pos settings
Number of Wideband Events
20
15
10
5
10
20
30
40
50
R in Inches
× neg. settings
o pos. settings
15%
10%
5%
Percent of Wideband Events
0
50
100
150
200
250
Momentum Setting

Figure 29

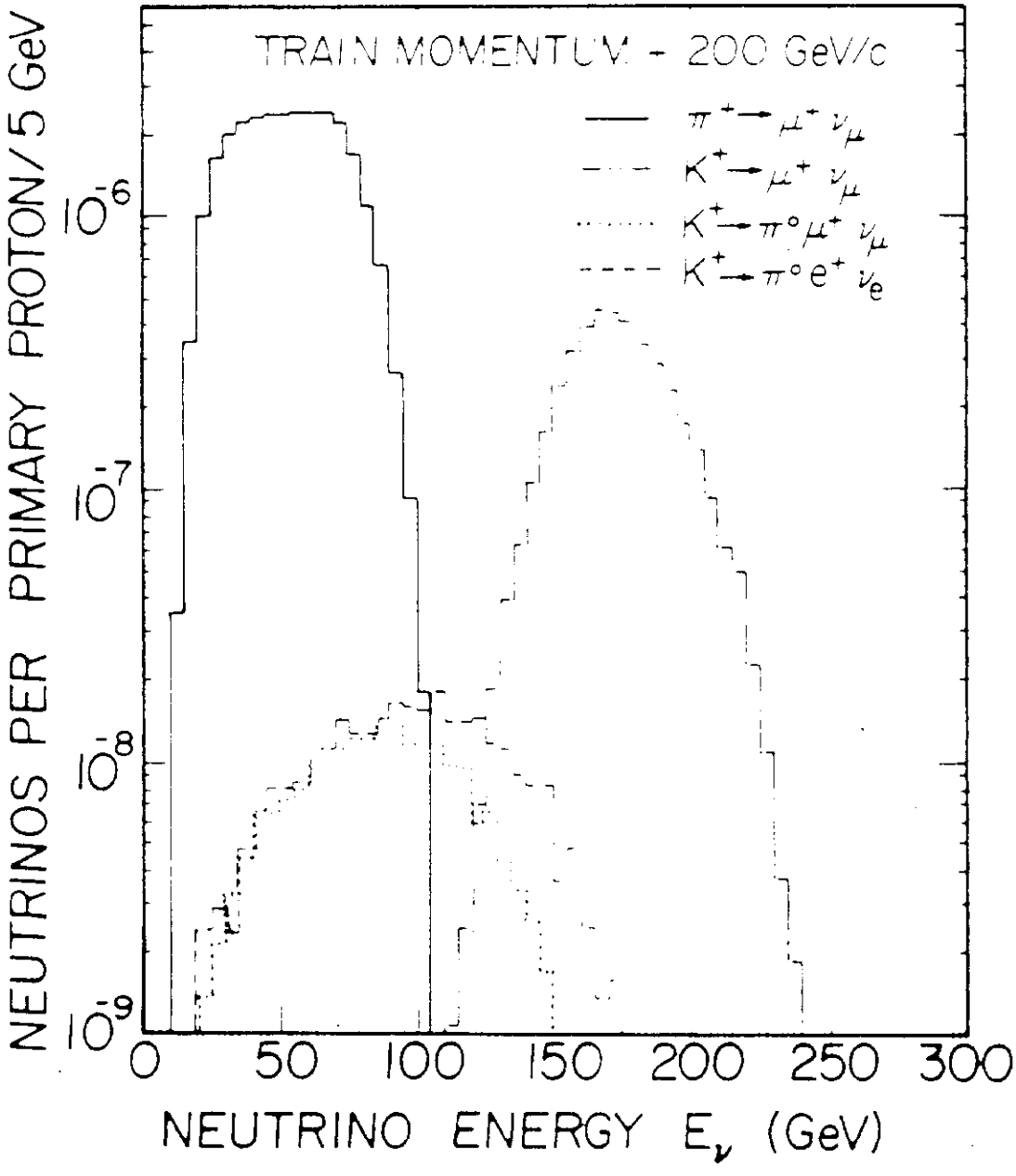
TRAIN MOMENTUM - 200 GeV/c
$\pi^+ \rightarrow \mu^+ \nu_\mu$
$K^+ \rightarrow \mu^+ \nu_\mu$
$K^+ \rightarrow \pi^\circ \mu^+ \nu_\mu$
$K^+ \rightarrow \pi^\circ e^+ \nu_e$
NEUTRINOS PER PRIMARY PROTON/5 GeV
10^{-6}
10^{-7}
10^{-8}
10^{-9}
0
50
100
150
200
250
300
NEUTRINO ENERGY E_ν (GeV)

Figure 30